# LIGHT PIPE DESIGN FOR SOLAR CONCENTRATOR

A Dissertation

by

CHEHAO HU

Submitted to the Office of Graduate and Professional Studies of
Texas A&M University
in partial fulfillment of the requirements for the degree of

DOCTOR OF PHILOSOPHY

| | |
|---|---|
| Chair of Committee, | Christi Madsen |
| Committee Members, | Kamran Entesari |
| | Laszlo Kish |
| | George Welch |
| Head of Department, | Miroslav Begovic |

August 2018

Major Subject: Electrical Engineering

# ABSTRACT

This dissertation includes three main sections: 1. Planar waveguide solar concentrator 2. Modeling light pipe scattering loss 3. Trade-off of the concentrator design. All of the simulations are accomplished by Zemax, TracePro, and Matlab. Each of this three software has their own advantages, for example, Zemax is handy to trace rays as several different conditions, TracePro has many professional built-in tools (e.g., Solar simulator), and Matlab allows more freedom of simulation.

In the first section, we discuss the first design of the planar waveguide solar concentrator in this world proposed by Karp, a design made by Liu that improves the Karp's first design, and a new design that satisfy the fabrication requirements. This new design achieves 30% of total harvesting efficiency under the low-DNI condition, 1000X concentration, 99.98% geometric efficiency, and 0.9° of acceptance angle.

In the second section, we go through the scattering loss of a light pipe and propose a new model to calculate the average scattering loss of a light pipe by the given RMS slope (m) of the surface. We demonstrate the RMS slope is a better indicator to represent the characteristics of a rough surface.

In the last section, we propose a new structure which improves the design shown in the first section, but the fabrication issues are not taken in to account. This structure has an extra lens above the waveguide to parallel the rays that enter the waveguide. By doing so to alleviate loss caused by HR coating and surface roughness. We also discuss the tradeoffs of using a compound parabolic concentrator and linear concentrator.

# DEDICATION

To my parents and wife

# ACKNOWLEDGMENTS

I would like to sincerely thank my research advisor, Dr. Christi K. Madsen, for giving me this chance to study in her group. Without her help, I might have given up this Ph.D. Degree. I would also like to thank other committee members, Dr. Kamran Entesari, Dr. Laszlo Kish, and Dr. George Welch, for their time throughout the course of this research.

I am fortunate to meet my previous groupmates, Yuxiao Liu and Ran Huang. I deeply appreciate their effort and devotion for this project. They taught me many skills and knowledge about optics. I am also grateful to have my current groupmates, Yusuf Dogan and Matthew Morrison. It is my pleasure to work with you.

Especially, I want to thank my parents and wife. They always support and help me to conquer every difficulty. Without their support, I can not be here.

In the end, I want to thank everything ever happened to me in this five years. No matter it is good or not, it makes me stronger.

# CONTRIBUTORS AND FUNDING SOURCES

## Contributors

This work was supervised by a dissertation committee consisting of Professor Christi Madsen, Professor Laszlo Kish and Professor Kamran Entesari of the Department of Electrical & Computer Engineering and Professor George Welch of the Department of Physics & Astronomy.

The sample used in the third section was provided by Yusuf Dogan, and one of the measurement was measured by Matthew Morrison.

All other work conducted for the dissertation was completed by the student independently.

## Funding Sources

Graduate study was supported by a fellowship from ARPA-E.

TABLE OF CONTENTS

Page

LIST OF FIGURES

Page

LIST OF TABLES

Page

# 1. INTRODUCTION

## 1.1 Solar energy

Solar energy is probably the oldest energy that human ever used, and it is one of the clearest and immeasurable energies. People have utilized the solar to dry salt, food, and clothes since thousands year ago, but the more efficient methods to utilize solar energy were presented in the last century. The current technologies to employ solar energy are solar heating, photovoltaics, solar thermal energy, solar architecture, and molten salt power plants. The photovoltaics is the most rapidly developed among all of these technologies.

The first solar cell was invented by Bell Labs in 1954, and the purpose was to provide the electric power to the people who live in the countryside. At the time, the solar cell is costly and low efficiency. The first solar cell is made of silicon, and its efficiency is only 6%. However, it was still a tremendous advance in human's history.

The ultimate goal of the development of the solar cell is to replace the traditional power, e.g., nuclear power and thermal power. Based on the report of 2000 World Energy Assessment by the United Nations Development Program, the annual potential of solar energy was 1,575–49,837 (EJ), and this value is several times larger than the total energy consumption of world (559.8 EJ in 2012) [1].

Currently, there are four major types of solar cell, e.g., multijunction, single-junction, thin-film, and crystalline Si. Multijunction cells have the highest efficiency, 46% [2], but it is also the most expansive type of solar cell. The silicon solar cells have lower efficiency, 27.6% [2], but it is relatively cheaper than multijunction cells. Hence, our goal is to find a new technology which can take advantage of this two type of solar cell, and also keep off their disadvantage.

## 1.2 Solar concentrator

### 1.2.1. Concentrator photovoltaics

Concentrator photovoltaics (CPV) is a technology that transfers sunlight to electric power by using the lens, a mirror or another optical component to focus sunlight onto a multi-junction photovoltaic (MJPV) cell. The main point is that utilize a cheaper optical component to reduce the demanded area of MJPV cell. A basic equation illustrates the cost of CPV [3] is defined as

$$\text{Cost}\left(\frac{\$}{\text{kWh}}\right) = \frac{C.C(\$/m^2) + \frac{Cell}{X}(\$/m^2)}{E_{in}(kWh/m^2 \cdot year) \times \eta_{sys}} \times ADR,$$

where C.C is the cost of the concentrator, Cell is the cost of the solar cell, X is the concentration ratio, $E_{in}$ is the total energy can be collected per $m^2$ in a year, $\eta_{sys}$ is the total system efficiency, and ADR is the annual discount rate. Based on this cost equation, the critical point to build a good CPV is to reduce the cost of the concentrator and increase the concentration ratio.

Although the CPV has many advantages such as high efficiency and low cost, it is still far less frequent than the conventional PV system. One of the reasons to cause this result is the volume of CPV. Unlike the conventional PV cell, CPV system includes the lens array and tracking system; these two component make it cannot be installed on the rooftop. There still exist other weakness for CPV, e.g., cannot fully utilize the diffuse sunlight, is sensitive to the shift of solar spectrum, and only can be used in the location with high direct normal irradiance (DNI). Therefore, Advanced Research Projects Agency-Energy (ARPA-E) announced the Microscale Optimized Solar-cell Arrays with Integrated Concentration (MOSAIC) Program [4] to solve the current disadvantages of CPV system in 2015. A successful CPV design in this project should possess the following properties:

- Overall harvesting efficiency in low-DNI $\geq 30\%$

- Optical efficiency of module >90% for DNI
- Geometric Concentration C ≥ 1000
- Overall module height < 25 mm
- Diffuse collection with efficiency >5% of incoming DIFF
- Acceptance angle ≥ 0.9°

1.2.2. Karp's first design

Various types of CPV were rapidly presented recently [5], e.g., flat reflector [6], Fresnel lens [7, 8, 9], or luminescent dot [10]. A novel type of CPC system, Planar Micro-optic Solar Concentration, was first proposed by Karp et al. in 2010 [11], as shown in Figure 1. Compare to the conventional CPV, all of the input sunlight will be collected by two cells in Karp's design. In this design, it includes a lens array, a planar waveguide, symmetric prism array, and two solar cell. The light is first collected by the lens array and then focused onto the small prism (with deposition of aluminum) that is located at the focal point of every lens. After the sunlight reflected by the prism, it will propagate inside of the waveguide through the total reflections (TIRs) and then collected by the solar cell.

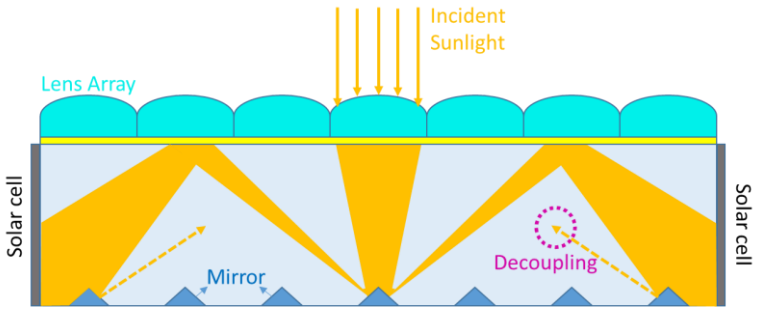


Figure 1. The side view of Karp's first design. Here, it only shows the light path from one lens.

The planar waveguide plays a critical role in this design; it considerably reduces the packaging process and provides a uniform output (no chromatic aberrations). However, this design has two inherent disadvantages. First, the light will be reflected by the prism several times when it is propagating inside of the waveguide. The number of reflections depends on the length and thickness of the waveguide. Every reflection on the prism may decrease the incident angle, and increase the chance to violate the TIR to cause some loss. Second, the reflectance of aluminum is lower than 90%; there always exist at least 10% loss in this system. Another weakness of this design is concentration ratio (500X); the concentration is restricted by the thickness of the waveguide. However, a thinner thickness will cause more intersections inside the pipe and then cause more loss.

1.2.3. Liu's design

Base on Karp's design, Liu proposed a new design in 2014 [12, 13], as shown in Figure 2. The basic structure of this design is similar to Karp. They both have a lens array, coupler (prism), the planar waveguide, and solar cell. Liu used the Fresnel lens and the tapered coupler to be the first and second concentrator, respectively. Every coupler has a 45° mirror, which redirects the sunlight into the channel waveguide. As the channel waveguides are placed side by side, light already coupled into the waveguides will not hit subsequent couplers, which avoids the decoupling issue associated with a slab waveguide. This design does not only keep the advantages from Karp's design (simplified packaging process and uniform output) but is also capable of achieving even 1000X concentration. Another remarkable feature in this design is this system can collect the diffuse sunlight by the silicon solar cell under the waveguide. Although this design solved the problems of Karp's design, it still has some issues, e.g., geometric loss and fabrication issues.

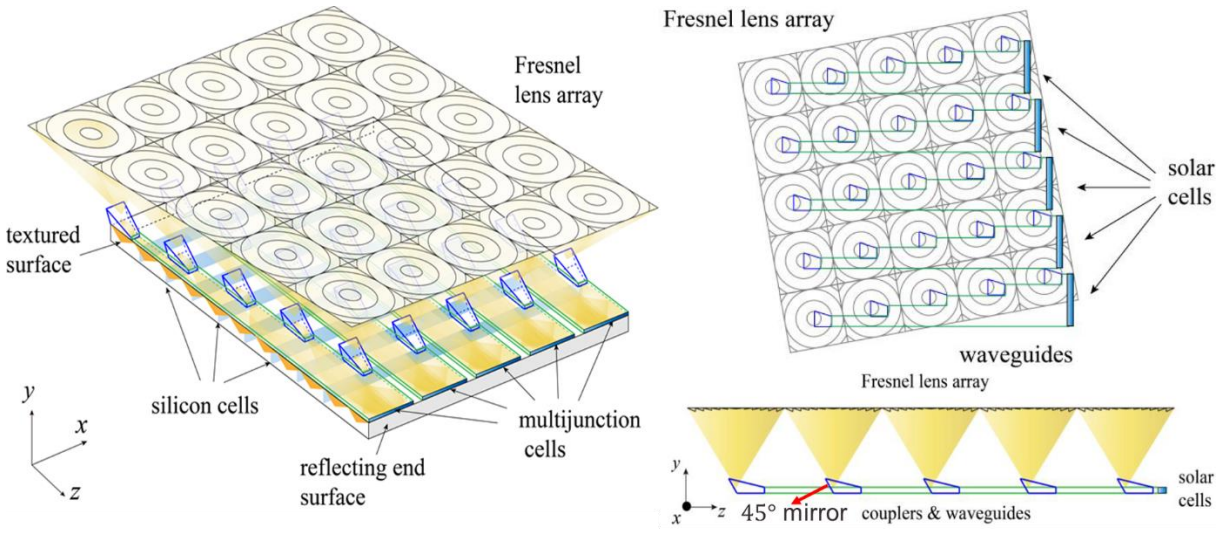


Figure 2. A waveguiding solar concentrator designed by Liu [12].

## 1.3 The scope of this work

An integrated CPV system includes optical components, photovoltaic cell, cooling system, and tracking system. The work shown in this dissertation mainly focus on the optical area, and it includes three parts:

- Improve the optical efficiency in Liu's design as the practical fabrication issues are considered.
- Propose a new model to calculate the average scattering loss in a light pipe.
- Presente another possible design that has different advantages from the previous design.

The details of optical design, other scattering models, and measurement setup are also discussed.

# 2. PLANAR WAVEGUIDE SOLAR CONCENTRATOR

Although Liu already solved the drawbacks of Karp's design, there are still three issues in Liu's design. First, his structure is unoptimized. The geometric efficiency of the whole optical component is 98.9%, but every percent is significant. Second, defective Fresnel lens. Ideally, Fresnel lens is a preferable choice for a CPV system. Nevertheless, it is hard to get a Fresnel lens with perfect quality. Third, surrounding material. This structure is designed as air surrounds it, but it is needed to be supported by a mechanical shelf. This section will go through the solutions by the following order, system overview, lens design tradeoffs, waveguide design, and overall system efficiency.

## 2.1 System overview

A small, 3x5 (lens element) prototype architecture is shown in Figure 3 to illustrate the essential components. It is composed of a lens array, waveguide array, MJPV cells, and an underlying Si PV cell. The red and yellow lines represent direct and diffuse sunlight, respectively. The direct sunlight is focused by each lens element onto a waveguide turning-mirror facet, whereby the direct light propagates through the waveguide to an MJPV cell. The diffuse light is not concentrated, but passes through the waveguide array and is collected by Si PV cells. Other low-cost, single-junction PV cells could be used for diffuse light collection as well.

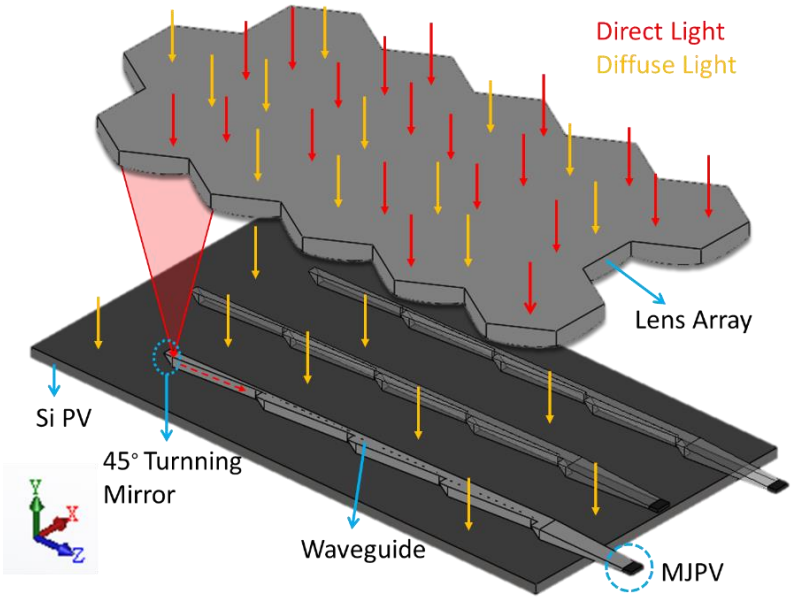


Figure 3. Schematic of a small, 3x5 lens-to-waveguide array prototype system, so that the components are easily visualized [14].

## 2.2 Lens design tradeoffs

Fresnel lens is frequently applied to the CPV system because of its thin thickness. However, it is not suitable for an optical system which requires high efficiency. The Fresnel lens is fabricated by the diamond turning process, and this process usually causes the rounded corner, nonvertical side edge, and higher roughness [15], as shown in Figure 4. Generally, these defects cause around 3% of the loss [16]. Therefore, a possible alternative is the aspherical lens, as shown in Figure 5. After optimizing the dimension of every component, this new structure has a geometric efficiency higher than 99.98%, but the thickness is 20 times thicker than Fresnel lens.

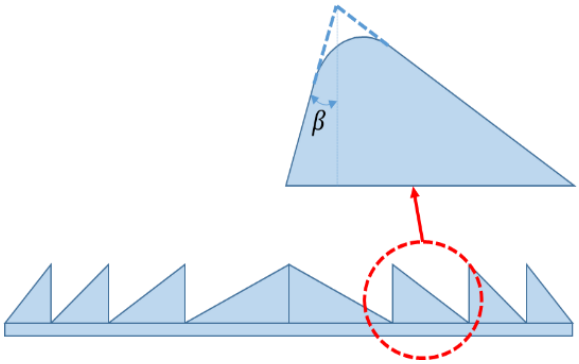


Figure 4. A diagram of the side view of a Fresnel lens. Usually, β is around 3°.

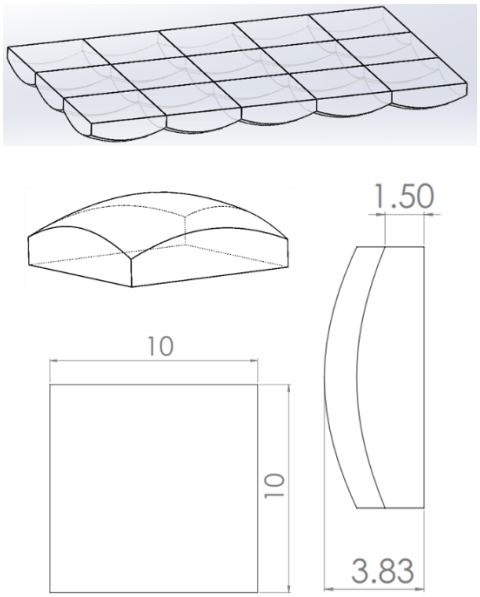


Figure 5. Schematic of a 10 x 10 x 3.83 mm square aspherical lens.

An ideal material for the lens array is low-loss glass. However, the cost and complexity of fabrication for a molded glass lens are relatively higher than PMMA. Therefore, the PMMA is still an attractive option. The PMMA has the disadvantage of higher absorption loss, which reduces the optical throughput. Based on the dimension shown in Figure 5, the average transmittance of a

square aspherical lens made by PMMA is 93% as using the solar spectrum. We maximized transmittance through the PMMA lens by reducing the necessary thickness of the lens. The best option here is to replace the square shape with a hexagon. For a given lens element area of 100 $mm^2$, the central thickness is reduced from 2.33mm to 1.84mm for a square and hexagonal lens shape (see Figure 6), respectively. This 21% reduction in thickness allows a 2.3% increase in lens transmittance for the optical path.

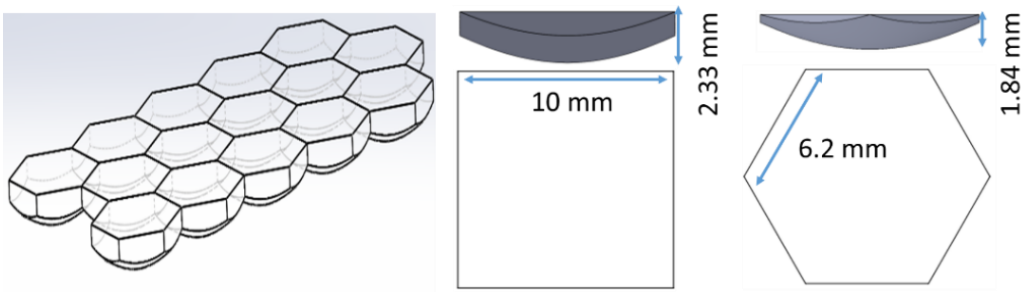


Figure 6. Compare to the square lens the hexagonal lens is 21% thinner, and it can be compactly connected with each other, too. The f# of the lens is 1.67 [14].

## 2.3 Waveguide design

In Liu's design [12, 13], every lens element only has a corresponding coupler, and this coupler is tapered in both X and Y direction (see Figure 7). Taper in Y direction decreases the incident angle on the upper and down surface, and it increases the chance to violate the TIR, especially when the bonding layer is not air. There are two possible ways to solve this problem, reduce the area of a bonding layer or find a material with a tiny refractive index, as shown in Figure 8. Nevertheless, these two ways are both hard to achieve. A better solution is to taper in Y direction later. (The lowest refractive index we found is 1.05 proposed by J.-Q. XI et al [17])

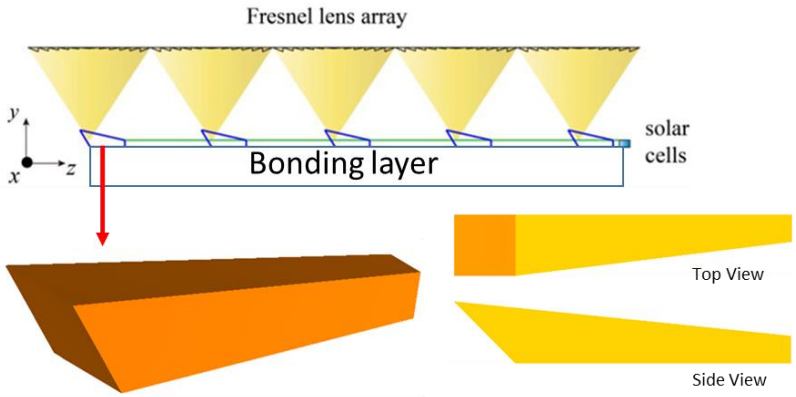


Figure 7. It is the side view of Liu's design, and the bonding layer in his design is air.

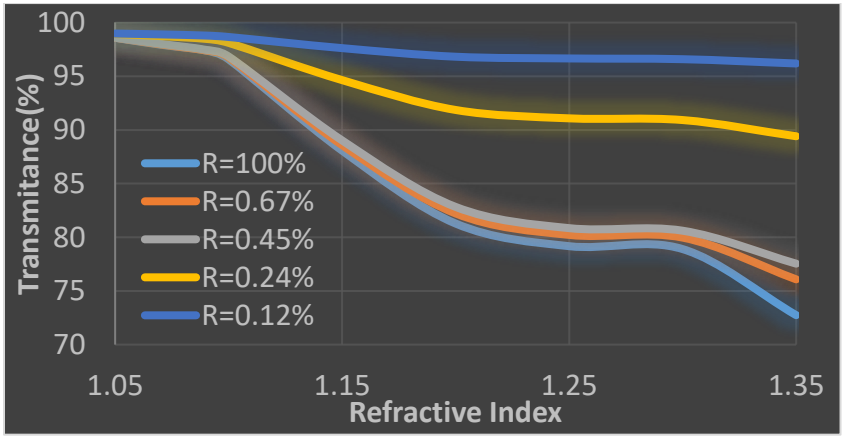


Figure 8. R is the ratio between the bonding layer and waveguide.

The newly designed waveguide includes three components: a first coupler, a slab channel and a second coupler (see Figure 9). The first coupler is tapered in the X direction, while the second coupler is tapered in the Y direction to achieve maximum concentration without violating a TIR condition. A gap is located between the first coupler and slab channel that prevents decoupling losses. The details dimension are shown in Figure 10. This new design scales to larger array sizes

as shown in Figure 11 with the full lens array aperture captured in the waveguide layer that is confined within the lens array area.

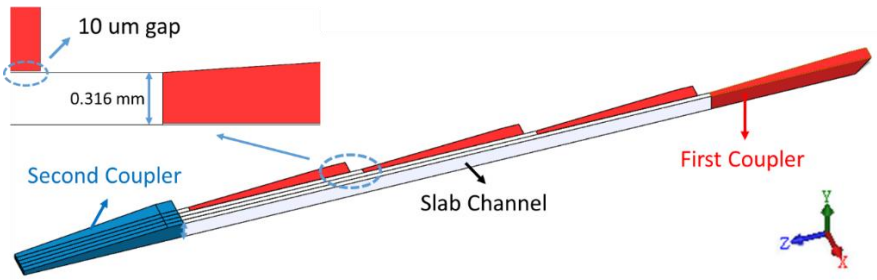


Figure 9. The red, white and blue color represents the first coupler, slab channel, and second coupler [14].

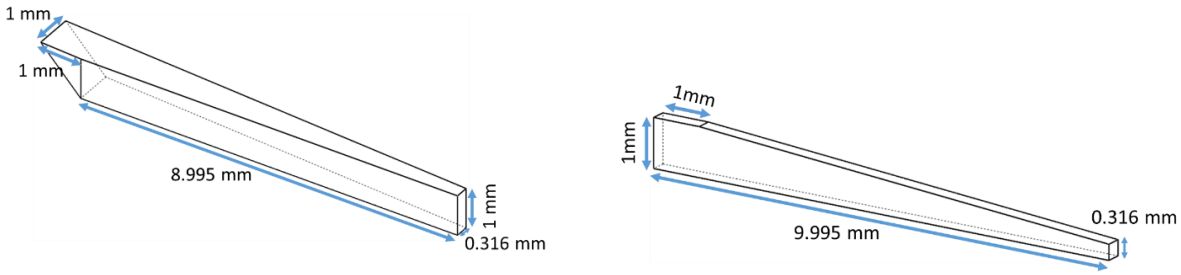


Figure 10. The up and down graph is the first and second coupler, respectively.

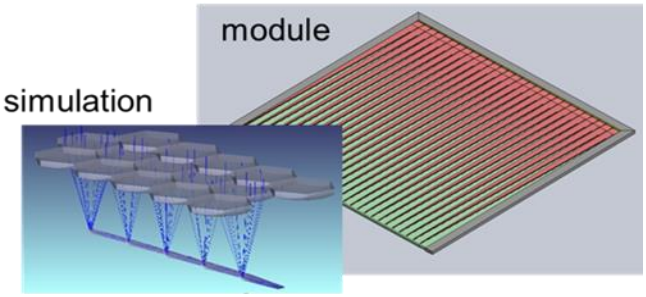


Figure 11. Simulation of one row of 5 lens elements coupling into a common waveguide section. A module view is showing the waveguides (in pink) coupled to a 28x28 lens element array [14].

The maximum number of coupling elements combined in a row will depend on the achievable waveguide loss and the ratio between the width of the waveguide and the length of the lens. The maximum number (N) of the lens in one row can be calculated by

$$N = \left\lfloor \sqrt{\frac{D^2}{W^2} - 1} \right\rfloor \text{ [15, 18]},$$

where D is the length of each lens or the distance between the center point of two adjacent lenses, and W is the width of the slab waveguide (see Figure 12). As D = 10.74 mm and W = 0.316 mm, the maximum N = 33, and $\theta = \sin^{-1}\frac{W}{D} = 1.686°$. By using fused silica, absorption losses are negligible, and we expect scattering loss to dominate. Figure 13 shows the simulation result using a scattering model, with parameters from our surface roughness measurements, in Zemax to model efficiency versus waveguide length. There is no geometric loss because there is no de-coupling mechanism in our design. These simulations predict that long lengths (up to 300mm) could be viable with high efficiencies (>95%) for the waveguide path.

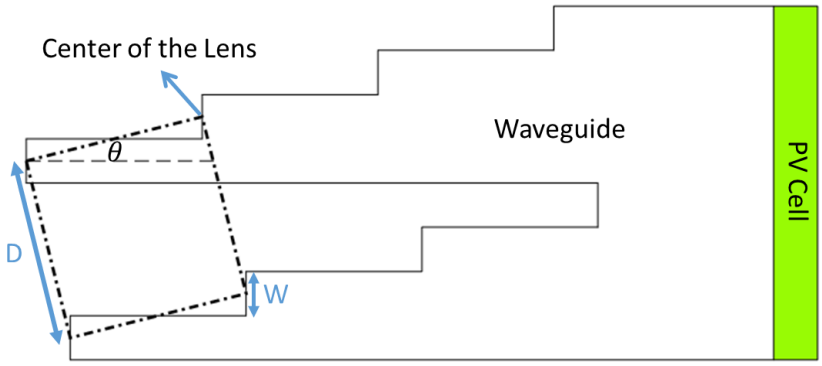


Figure 12. A top view of a waveguide for a 2 X 4 lens array. The scale of this graph is not exactly correct.

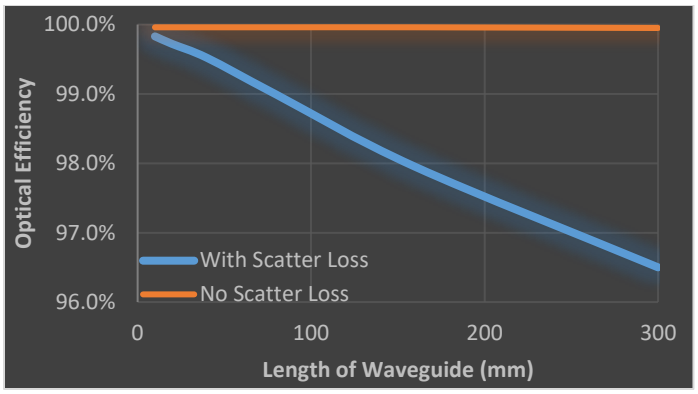


Figure 13. Comparison of the waveguide path optical efficiency without scattering loss and with scatter loss [14].

The distance between the lens and waveguide arrays is about 20mm, so the design is quite compact (<1inch total thickness). Under these constraints, we optimized the lens design and showed an improved incidence angle (tracking) tolerance compared to Liu's design in Figure 14. The blue line and red line represent the new and old design, respectively. The incident angle tolerance is almost ±1˚ at 90% optical efficiency.

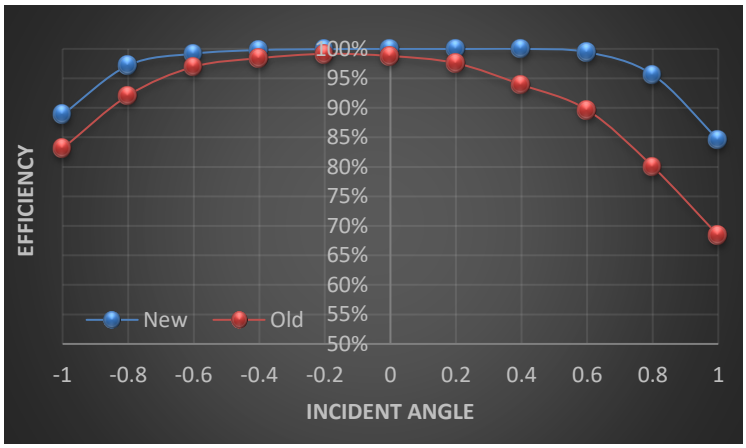


Figure 14. Incident angle tolerance for the new and previous designs [14].

## 2.4 Diffuse light collection

Diffuse light constitutes a significant portion of total sunlight. Hence, higher total solar harvesting efficiency requires the collection of diffuse light. We use the Zemax and TracePro to simulate the performance of diffuse light capture in our optical system. We followed two steps to simulate diffuse sunlight: 1) we used a swept-angle source approach in Zemax, and 2) an atmospheric model in TracePro to get an angular distribution.

1) Swept-angle source: Based on Figure 15, we collect the rays which hit detector 2, and increased the tilt angle of the source from $0^{\circ}$ to $90^{\circ}$. The average loss is around 14% due to the reflection of the lens (see Figure 16).

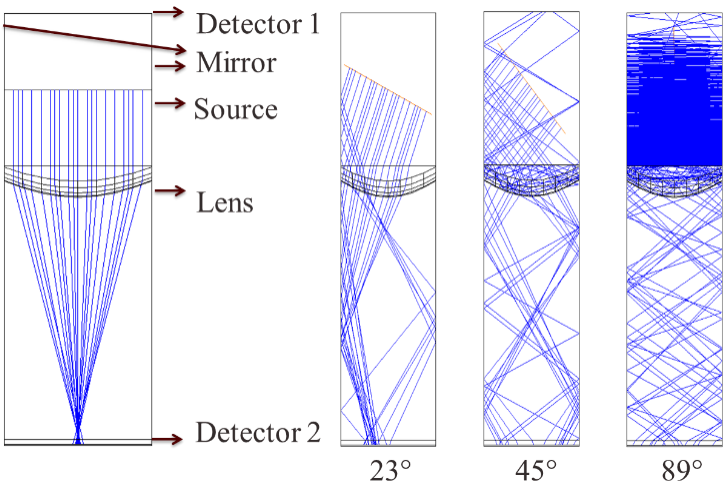


Figure 15. Swept-angle diffuse light simulation [14].

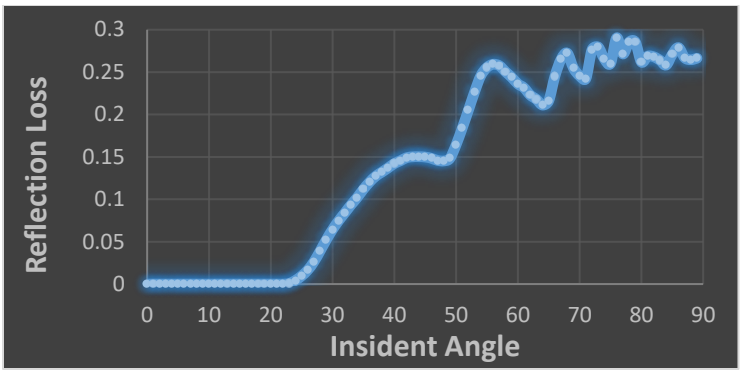


Figure 16. The graph of reflectance versus incident angle. Here, the Fresnel reflection loss is ignored; only back reflection from the lens is considered.

2) To simulate the angular distribution of a given atmospheric model, we used TracePro's "Solar Emulator" tool, which can simulate the sun in any location and weather. We tested for Singapore under partly cloudy conditions with the Igawa All sky model. The simulation structure is shown in Figure 17(a). Applying the sky model inside of the red circle, we placed a mask under the source to block the direct light and built a wall around the system to make sure the only entrance of diffuse light is the lens. Figure 17(b) shows the light that reaches the Si PV.

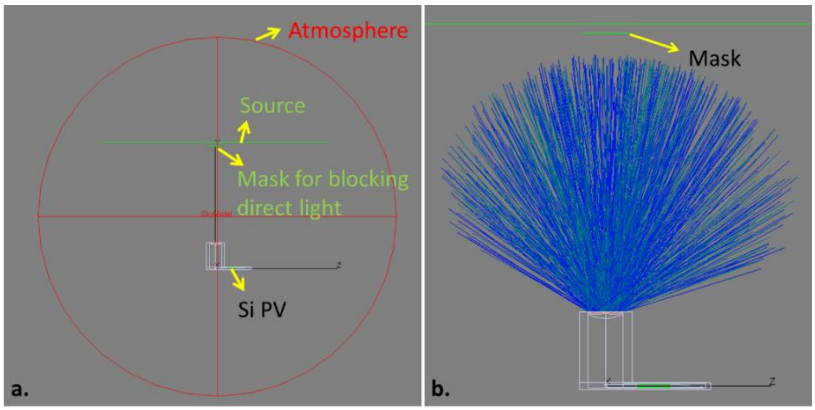


Figure 17. (a) Simulation structure setting. (b) Visualization of the angular distribution [14].

Collecting the diffuse light on the Si PV provides the angular distribution, shown in Figure 18. Then, we weighted the efficiency versus tilt angle from step 1 by this angular distribution. The average diffuse optical path loss is estimated at 5.7% using this approach.

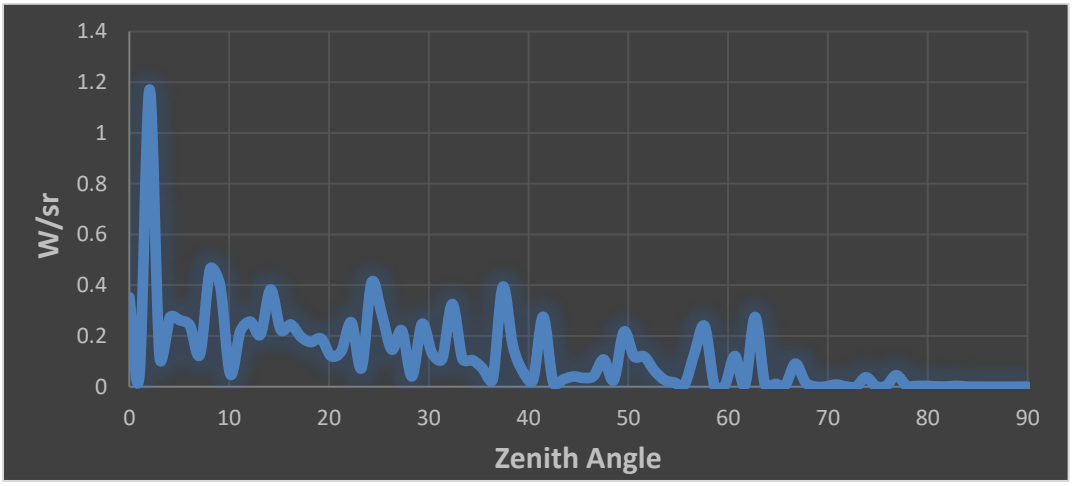


Figure 18. The angular distribution of diffuse sunlight [14].

## 2.5 Overall system efficiency

Until here, we have shown the solutions that solve the defects in Liu's design and also optimized the optical performance. This new design possesses 1000X concentration ($\frac{Area_{lens}}{Area_{output\ aperture}} = \frac{2\times\sqrt{3}\times 5.37^2}{0.316^2}$), height < 25 mm, and acceptance angle > 0.9°. Now, we are going to check if this system can achieve 30% of total harvesting efficiency under the Low-DNI condition. The total harvesting efficiency is defined as

$$\eta_{total} = \eta_{direct} + \eta_{diffuse}$$

$$\eta_{direct} = 60\% \times \eta_{optic} \times \eta_{MJPV}$$

$$\eta_{diffuse} = 40\% \times \eta_{optic} \times \eta_{siPV}$$

$$\eta_{optic} = \eta_{geometric} \times \eta_{AR} \times \eta_{HR} \times \eta_{scattering}$$

The total harvesting efficiency ($\eta_{total}$) includes two parts, one is from direct sunlight ($\eta_{direct}$) and another is from diffuse srunlight ($\eta_{diffuse}$). Each of $\eta_{diffuse}$ and $\eta_{direct}$ is equal to the whole system optical efficiency ($\eta_{optic}$) multuplied by efficiency of solar cell. Here, we assume the fraction of direct sunlight is 75% and 60% for High-DNI and Low-DNI, respevtively. $\eta_{optic}$ includes the transmitance of anti-reflection (AR) coating, hifh-reflection (HR) coating, optical structure, scattering, and any other possible issues that could decrease the transmitance.

Before we consider the real case in the efficiency budget table, we have to check if our calculation for the efficiency of PV cell is correct. Table 1 shows the needed parameters for calculating efficiency under an ideal condition. We choose the MJPV cell (3-C44) with 42.9% efficiency under 1000X concentration from AZUR SPACE [19], and the PV cell (C60) with 21.5% efficiency from Sun Power [20]. Because some of the parameters that are needed for calculation of the solar cell efficiency are not from the datasheet of the cell, so we have to slightly adjust them to get the same value of efficiency shown in the datasheet. For example, we reduced the $V_{oc}$ from 3.13 V to 3.1 V and from 0.71 V to 0.693 V for MJPV and PV, respectively. Then we got 42.82% for MJPV and 21.48% for PV; they are almost the same as the value shown in the datasheet.

Table 1. The efficiency table under the ideal condition.

| ID | Photovoltaics | | | | | | |
|---|---|---|---|---|---|---|---|
| 1 | Hexagonal Lens (Acrylic Copolymer)<br>Thickness = 2.75 mm | Direct | | | | | Diffuse |
| 2 | | MJPV | | | Total | | PV |
| 3 | Parameter or Component | SR1 | SR2 | SR3 | Series | Parallel | SRD |
| 4 | Material | GaInP | GaInAs | Ge | | | Silicon |
| 5 | Wavelength (nm) | 350-681 | 681-935 | 935-1795 | | | 350-1150 |
| 7 | PV Junction Voltage, Voc(V) | 1.56 | 1.13 | 0.41 | 3.1 | | 0.693 |

| | | | | | | | |
|---|---|---|---|---|---|---|---|
| 8 | Input Optical Power Density(W/m²) | 375.92 | 234.05 | 243.00 | 853.0 | 853.0 | 946.3 |
| 9 | Input Current Density (A/m²) | 162.00 | 149.88 | 245.31 | 557.19 | 557.19 | 441.49 |
| 12 | QE of MJPV&PV (3J-Spectrolab) | 0.835 | 0.895 | 0.685 | | | 0.840 |
| 13 | Optical Transmission (%)* | 100.00 | 100.00 | 100.00 | | | 100.00 |
| 14 | Current density (A/m²) after Optical Transmission & MJPV QE Losses | 135.3 | 134.2 | 168.1 | 134.2 | 437.55 | 370.88 |
| 15 | Output Electrical Power Density (W/m²) | 211.0 | 151.6 | 68.9 | 416.0 | 431.6 | 257.0 |
| 16 | PV Fill Factor (FF)(%) | 87.8 | 87.8 | 87.8 | 87.8 | 87.8 | 79.1 |
| 17 | Efficiency (%) | 49.29 | 56.89 | 24.90 | 42.82 | 44.43 | 21.48 |
| 18 | Efficiency of MJPV&PV (Target)(%) | | | | 42.90 | | 21.5 |

Table 2 shows the transmission of every component and surface under a real case. It considers the material absorption, AR and HR coating from OFS Optics, diffuse sunlight, and waveguide loss. Here, the system can accept 9% of waveguide loss, which includes scattering loss and other possible issues, and still can achieve 30% of total harvesting efficiency in Low-DNI condition.

Table 2. An optical path efficiency table. Apply the optical transmission get from this table to Table1 to calculate the total efficiency. For achieving 30% of total efficiency under the Low-DNI, we assume the maximum loss from the waveguide is 9%.

| Optical path efficiency budget | | | | | |
|---|---|---|---|---|---|
| | MJPV | | | Total | SiPV |
| Transmission of Lens | 97.7% | 98.8% | 90.6% | 94.9% | 98.2% |
| AR Coating: Surface 1 | 99.1% | 99.1% | 94.5% | 97.9% | 95.0% |
| AR Coating: Surface 2 | 99.2% | 99.0% | 94.4% | | 98.0% |
| AR Coating: Surface 3 | 98.3% | 98.3% | 93.5% | | |
| 45° Surface | 95.73% | 97.43% | 95.66% | 96.16% | |
| Waveguide transmission* | 91.0% | 91.0% | 91.0% | 91.0% | |
| Diffuse Transmission | | | | | 87.6% |

| | | | | | |
|---|---|---|---|---|---|
| Optical transmission | 82.25% | 84.49% | 65.90% | 77.8% | 80.1% |

| Summary of High and Low-DNI Efficiencies | | | | |
|---|---|---|---|---|
| Efficiency of Direct & Diffuse(High-DNI) | 0.250 | 0.268 | 0.272 | 0.054 |
| Total Efficiency(High-DNI,75%) | 0.322 | | | |
| Efficiency of Direct & Diffuse(Low-DNI) | 0.200 | 0.214 | 0.217 | 0.086 |
| Total Efficiency(Low-DNI,60%) | 0.3003 | | | |

## 2.6 Summary

Our new design provides high concentration (1000x) and almost perfect geometric optical efficiency, 99.9%. In addition, this architecture can collect substantial diffuse light (94.3% simulated for one location so far). If operating this system with a 43% efficiency MJPV and 20% efficiency Si PV, the maximum solar harvesting efficiency can achieve 33% under 30% diffuse conditions (70% DNI) with assuming 9% waveguide loss. We have demonstrated the basic building blocks to achieving an optical path with 90% efficiency or more.

# 3. MODELING LIGHT PIPE SCATTERING LOSS

## 3.1 Introduction

Highly multimoded waveguides, or light pipes, are used for transmitting light from a variety of sources, from solar to lasers and LEDs. For light pipe applications such as concentrating solar photovoltaic or thermal systems, the desire is to make the light pipe transmission as close to unity as possible, i.e., minimizing outcoupling by scattering due to surface roughness.

For simulating the rough surface, we have several models can use, e.g., Lambertian, Gaussian, PSD, K-correlation, Harvey-Shack, and ABg model [21]. Each of them has their own suitable situation, people have to find which one can correctly describe the behavior of the stray light for the sample, and all of these models require knowledge of the bidirectional scattering distribution function (BSDF [22]). However, BSDF is challenging, sample dependence and time-consuming. Furthermore, it is an experimental measurement of the ratio between input and output power, so it is a proper method to simulate scattering light for a measured sample but not to predict an unknown sample. Another drawback of BSDF is that BSDF is interaction data between an incident beam and a small piece of the sample, it cannot guarantee the remaining part of the sample has the same behavior, especially when the sample is a long light pipe.

Therefore, we want to develop a fast and universal algorithm to approximate the outcoupling loss inside of a light pipe. For achieving this goal, we resurvey the parameters that people are using to describe a rough surface, and we observed RMS slope (m) is a better general predictor of outcoupling loss for both periodic and random surfaces rather than spatial frequency ($\Lambda$) and RMS roughness ($\sigma$). Using RMS slope to characterize the loss provides much wider acceptability of surface roughness, and both m and $\sigma$ are easy to get directly from the surface

height profile measurement or power spectral density (PSD). In Bergström's [23] and Baghsiahi's [24] paper they also mention the similar point.

3.2 Theoretical background

Before we start to trace the rays inside of the light pipe, we need to know the mechanisms when the light hit onto a rough surface. Remillard [25] discussed five loss mechanisms in the light pipe: intrinsic absorption, bulk scattering, roughness at the core-cladding interface, defects at the core-cladding interface and absorption in the cladding material. Here, we only focus on the loss due to a rough interface. In Remillard's paper [25], the reflectivity (R) is given by $R=R_0\times\exp[-(2\kappa\times\sigma)^2]$, where $R_0$ is the Fresnel equation, $\kappa=2\pi n_{co}\cos(\theta)/\lambda$, $n_{co}$ is the refractive index of the core layer, $\theta$ is the local incident angle, and $\lambda$ is the wavelength of the source. This equation only can be applied to a slightly rough surface; it means $4\pi\sigma\cos(\theta)/\lambda \ll 1$. Actually, if the surface satisfies this criterion, then the exponential part in R will close to one. It means that we can only consider Fresnel equation for reflectivity even as $\sigma \ll \lambda$. Furthermore, if the complexity of testing circumstances is high or the reflection times are high, then we can even only consider total internal reflection (TIR) condition.

In this dissertation, we employed the geometric optics (GO) approximation to trace the rays inside of the light pipe. The GO approximation is an approximation of electromagnetic wave theory, and Tang [26, 28] proposed that to get a good comparison with the wave-theoretical methods the GO approximation is restricted by $\sigma\cos(\theta_{in})/\lambda > 0.17$ and $\sigma/L_c < 2.0$, here $\theta_{in}$ is the incident angle and Lc is the correlation length. By combining the conclusions from Remillard's and Tang's paper, we can refer that GO approximation can be applied to a wide range of $\sigma$. Therefore, all of the simulation in this dissertation only considers the Snell's law and Fresnel

equation at the intersection, and we simulated random and periodic surface for both 2-D and 3-D, and then gather the statistics.

### 3.3 2-D simulation

A rough surface can be specified by RMS roughness, correlation length and autocorrelation function. We built a 2-D light pipe with one rough surface in Matlab, as shown in Figure 19, and employed the algorism presented by Bergström et al [29] to control the rough surface. The Matlab pseudo code of creating a 2-D rough surface is written as:

Input: N - number of surface points

L - length of surface

h - RMS height

cl - correlation length

Output: f - surface heights

x - surface points

```
x = linspace(-rL/2,rL/2,N);
Z = h.*randn(1,N);
F = exp(-x.^2/(cl^2/2));
f = sqrt(2/sqrt(pi))*sqrt(L/N/cl)*ifft(fft(Z).*fft(F));
```

Here, the autocorrelation function used is Gaussian distribution. For satisfying the Nyquist sampling theory and achieving sufficient Gaussian statistics, we have to follow the inequality: $L/500 > L_c > 2L/N$, L is the length of pipe and N is the number of sampling point. By making the $L_c$ = 0.03, 0.04 and 0.05 mm, we create three different surfaces which have the same σ, 1.3 μm, and the corresponding m = 0.06, 0.0456 and 0.0366, as shown in Figure 20. The basic shape of these three curves are the same, but longer $L_c$ creates a smoother curve.

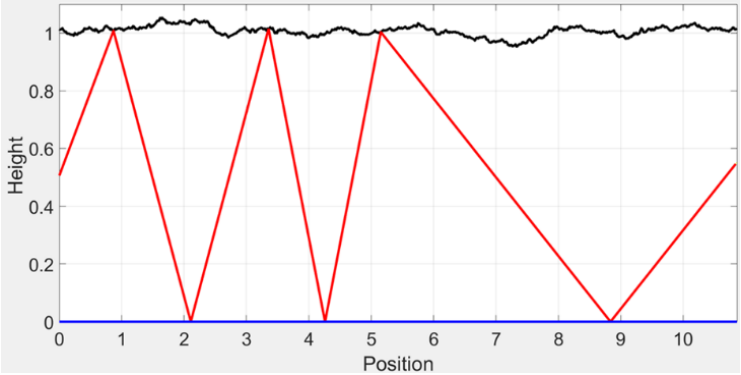


Figure 19. The black line is the rough surface, the red line is the ray, and the blue line is a perfect specular surface.

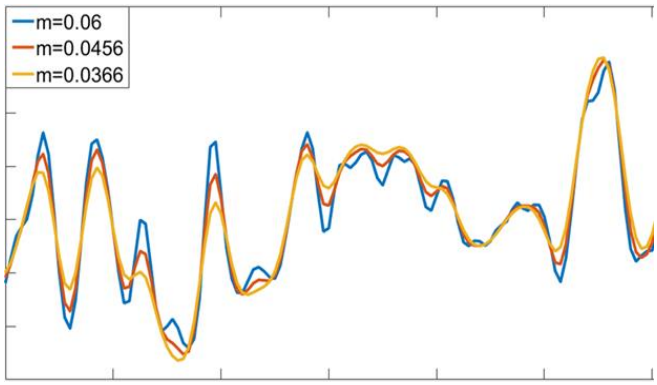


Figure 20. 2-D rough surfaces with σ = 1.3 um and m = 0.06, 0.0456 and 0.0366.

For the ray tracing part, we work out the intersection between the incident ray and the facet of the surface, and calculate the transmittance by Fresnel equation. Here, if the X component of the reflectional ray vector is minus, then we assume its transmittance is zero. Since this ray tracing simulation assumes discrete rays (or a point light source), we do not get satisfactory surface statistics if we only simulate once. Therefore, we simulate 3000 times and average the loss, i.e., we create 3000 different surfaces with the same RMS slope, trace only one ray for each surface, and average the loss. Figure 21 shows that even though the surfaces have the same RMS roughness,

their average losses are still different if their RMS slope is not the same. Figure 22 views this phenomenon from another angle, but it still shows the same conclusion as shown in Figure 21. Figure 22 shows a loss versus incident angle plot for three different surfaces with the same RMS slope, 0.03, and σ=0.656μm, 1.28μm and 21.38μm. These two figures show that no matter what the RMS roughness is if two surfaces have the same RMS slope, then they will have the same (average) scattering loss.

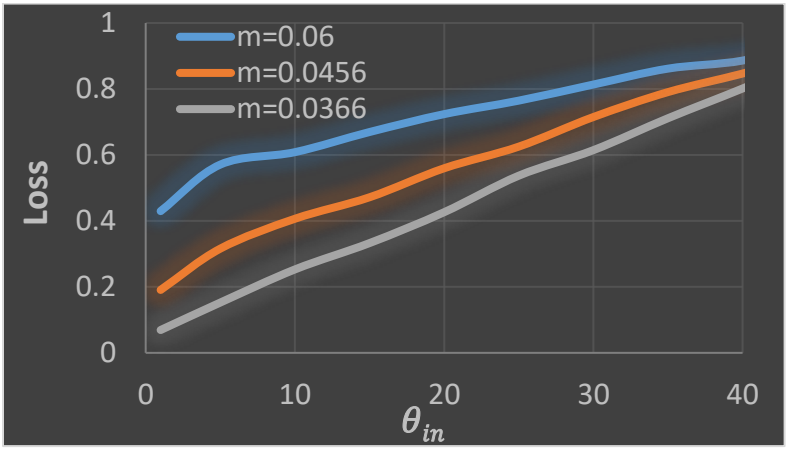


Figure 21. Here, σ = 1.3 μm, L = 100 mm, $n_{cladding}$=1 and $n_{core}$=1.49.

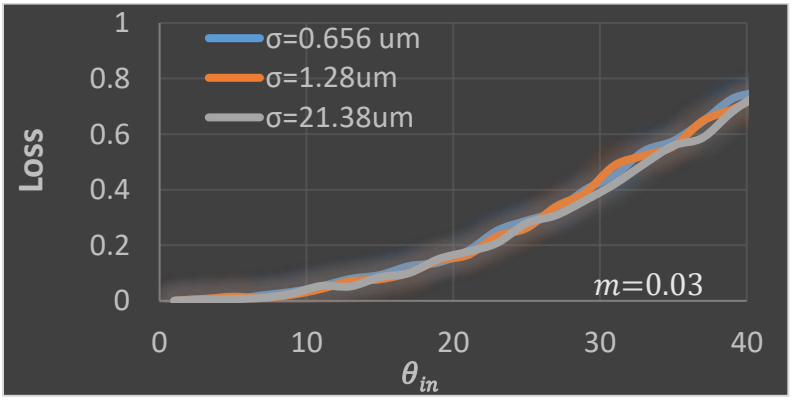


Figure 22. Here, m = 0.03, L = 100 mm, $n_{cladding}$=1 and $n_{core}$=1.49.

For inspecting our Matlab simulation, we build a similar testing system in Zemax. First, we create two identical "polygon objects" that both have one wavy rough surface, as shown in Figure 23, rotate one of the objects along Z-axis by 180°, combine these two objects to get a light pipe with two wavy rough surfaces, then import it to Zemax. For making the testing condition of this 3-D simulation close to a 2-D simulation of Matlab, we confine the incident angle of light source only can change on the Y-Z plane (from 2° to 21°). When L=40mm, height = 1 mm, m = 0.06, $n_{cl}/n_{co}$=1.31/1.45 and with two rough surfaces (top and bottom), the simulation result from Zemax and Matlab are almost the same (see Figure 24). Because we cannot create 3000 different objects and import all of them to Zemax, hence we need to increase the size of the light source to get sufficient statistic data of the surface in Zemax. However, this increase in the size will cause some error because the total propagation distance is different for every ray that starts at different Z position, but this effect caused by a small deviation of distance can be ignored as $\theta_{in}$ or L is large. Figure 24 also compares the simulation result between the Gaussian beam and collimated beam, and they agree well with each other.

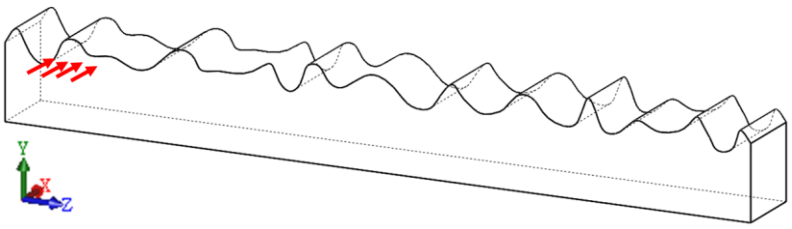


Figure 23. A diagram of the light pipe with one rough surface and the incident angle of light only changes on Y-Z plane.

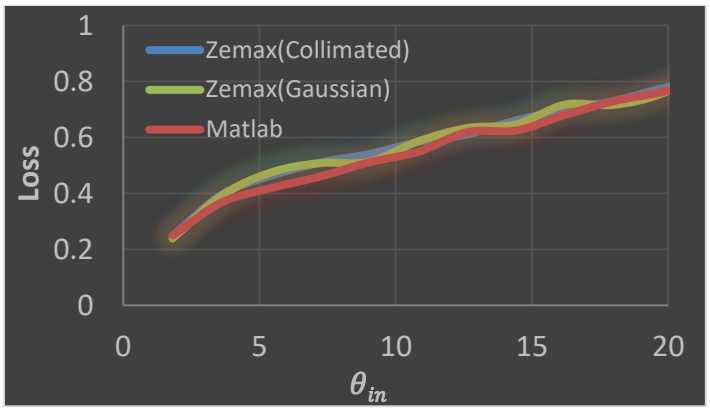


Figure 24. Comparison of scattering loss between Zemax and Matlab.

The 2-D periodic surface is also investigated. A sinusoidal surface is created (see Figure 25) by length = 60 mm, amplitude = 0.002 mm, $n_{cl}$ = 1, and $n_{co}$ = 1.5. As the random surface simulation, we need to simulate it 3000 times, but by controlling the phase of the sin wave. The results are shown in Figure 26. Figure 27 shows Comparison between random and period surface as m = 0.03. In conclusion, all of the 2-D simulation results is expressing the same concept; the RMS slope dominates the scattering loss no matter what the surface roughness, spatial wavelength or the distribution of surface profile is.

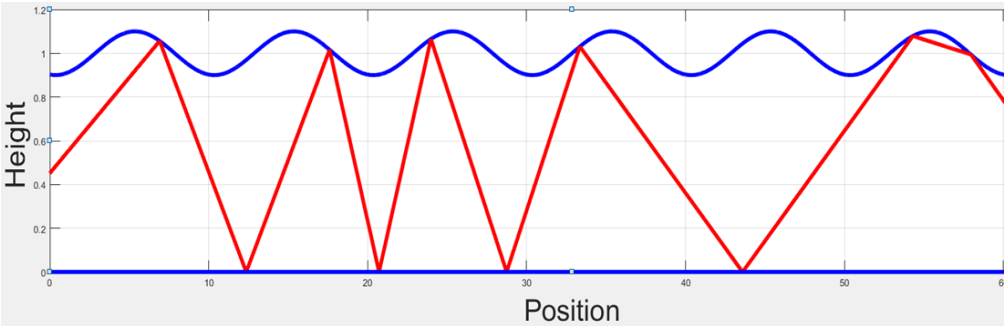


Figure 25. A light pipe with a sinusoidal surface as length = 60 mm.

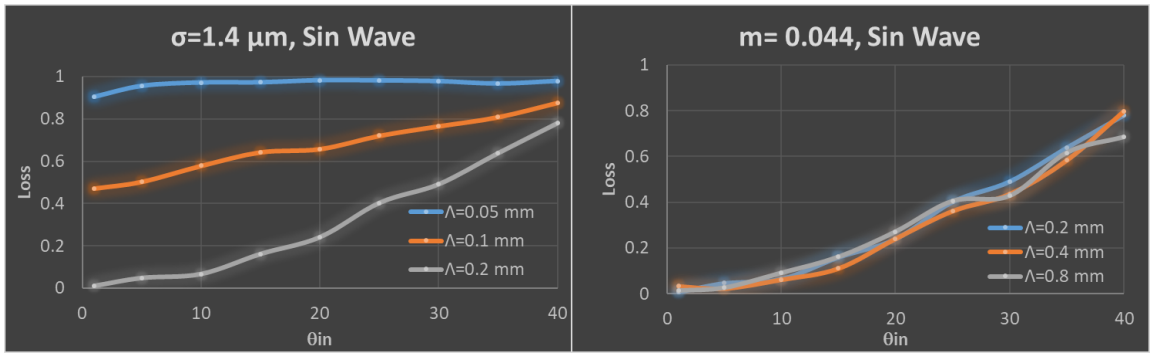


Figure 26. 2-D scattering loss simulation as σ = 1.4 μm (left) and m = 0.044 (right). Λ is the spatial wavelength or the period of the sin wave.

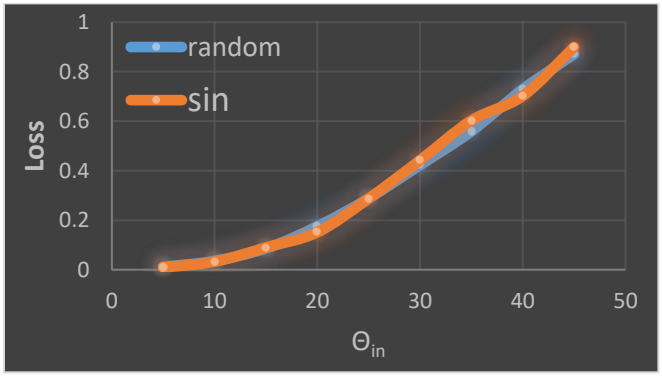


Figure 27. Comparison between random and period surface as m = 0.03.

## 3.4 3-D simulation

In the previous subsections, we proofed that RMS slope dominates the scattering loss no matter what the roughness and spatial period are in the 2-D pipe. Now, we want to investigate if this concept can be applied to the 3-D pipe. The testing system is shown in Figure 28, and it includes a source with $\theta_{in}$ = 0.38sr, a light pipe, and a detector. We utilize a function name Reptile in TracePro to create a periodic surface, and then detect the output power at the end of the pipe. We create three different shapes of square tile (triangle, pyramid, and sphere), and then construct

a rough surface by repeatedly put the same shape of tile on the light pipe, see Figure 29. In this simulation, we create four sizes (spatial period (Λ) = 10, 100, 500 and 990 μm) for every shape of the tile. The results of ray tracing are shown in Figure 30. For the same shape and RMS slope, different Λ means different RMS roughness, so from Figure 30 we can observe that if light pipes have the same RMS slope, then their loss will be the same just like the conclusion gotten from 2-D simulation even their surface has a different shape of the tile. Figure 30 also shows the comparison of loss between different tile as Λ = 10 μm, and there is no an apparent difference between them.

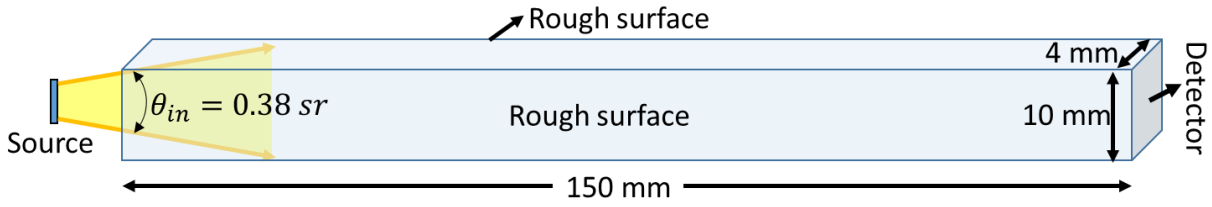


Figure 28. The testing system includes a source with $\theta_{in}$ = 0.38 sr, a 4 x 10 x 150 mm light pipe and a detector, and this pipe has two rough surfaces [27].

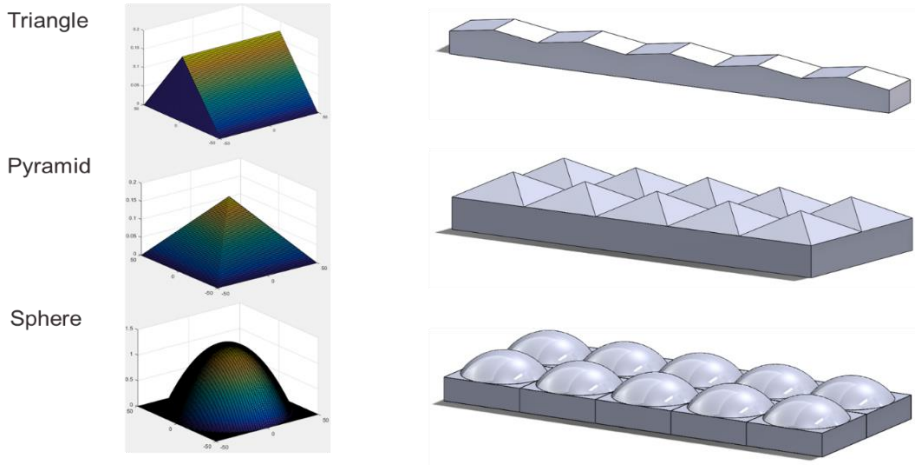


Figure 29. Examples of periodic surface texturing (triangle, pyramid, and sphere) [27].

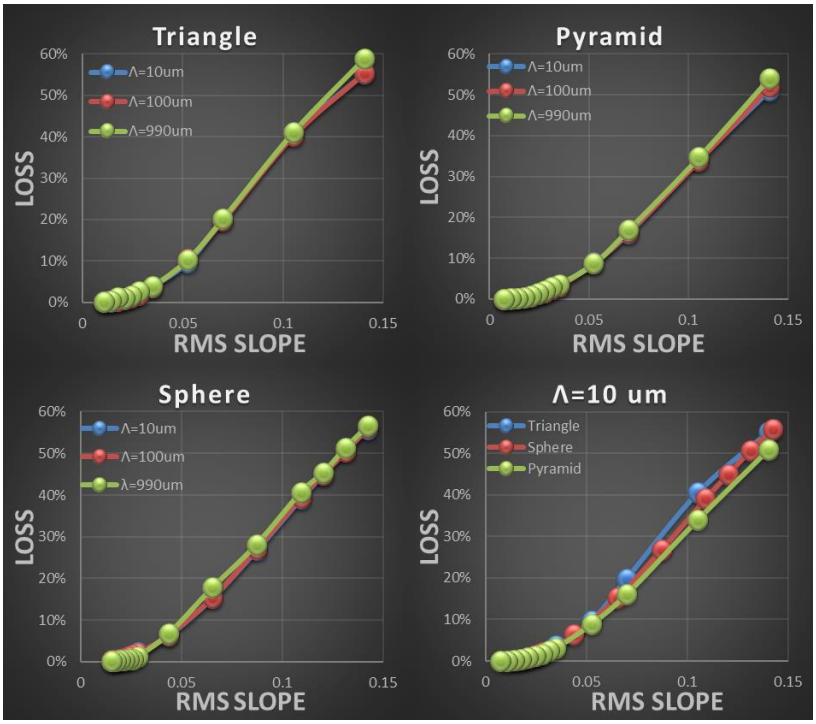


Figure 30. Simulation of outcoupling loss plotted versus slope for periodic surface texturing [27].

The 3-D random surface was also investigated. As the 2-D simulation of the random surface, we created a 3-D polygon object and analyzed it by both Zemax and Matlab. The Matlab pseudo code of creating a 3-D rough surface is written as [29]:

Input: Nx & Ny - number of surface points for X and Y axis, respectively

Lx & Ly - width and length of the surface, respectively

h - RMS height

clx & cly - correlation length for X and Y axis, respectively

Output: f - surface heights

x - surface points

```
x = linspace(-rL/2,rL/2,N);
Z = h.*randn(Nx, Ny);
```

F = exp(-((X.^2+Y.^2)/(clx^2/2)));

f = 2/sqrt(pi)*sqrt(Lx*Ly/Nx/Ny)/clx*ifft2(fft2(Z).*fft2(F));

The schematic plot of Matlab 3-D simulation process is shown in Figure 31. The main process is the same with 2-D simulation, but the ray tracing part is more complex. After the surface is created, classify the first surface the ray will hit. If the first reflective surface is the output surface ( surface 5), then the transmittance (T) equal to 1 and restart a new run. If the first reflective surface is the side wall (surface 1-4), then work out the reflection point and the ray vector (V). If the Y component of the ray vector is larger than zero and the incident angle on the surface is larger than the critical angle, then go back to the second step to find the next reflective surface. If the ray violates the TIR condition or the Y component of the ray vector is smaller than zero, then the T will be 0. Keep running this process utile T is 0 or 1 for 5000 times, and average the loss.

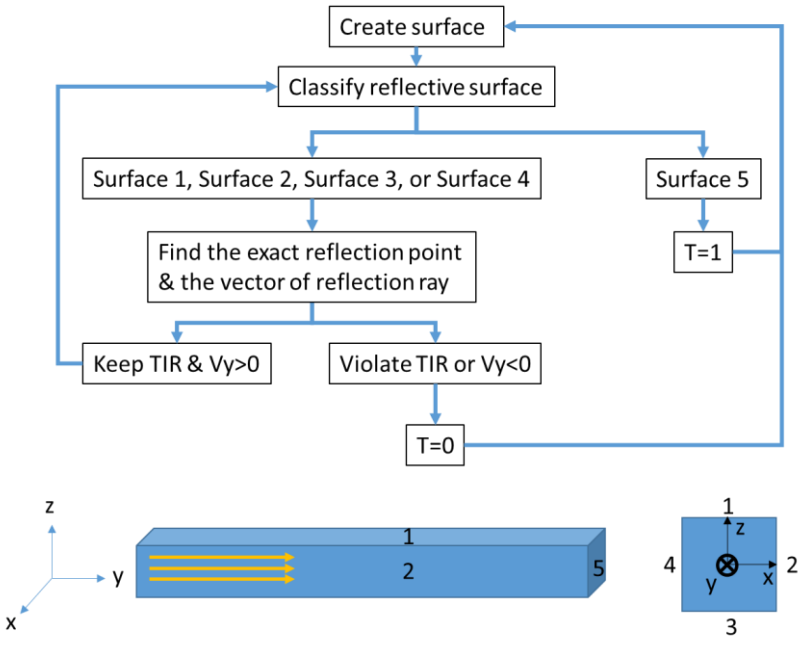


Figure 31. A schematic plot of Matlab 3-D simulation process. Vy is the Y component of the ray vector. The input surface is surface 6.

The top view of a 3-D random surface looks like a grid (see). The first step for tracing the ray is to find the facet hit by the ray. There are two ways to classify the surface by four points, e.g., connect P1 and P3, or P2 and P4. In this simulation, we define the reflective facet based on the most close grid point. For example, if the ray hit on the surface which is composed of P1, P2, P3 and P4, and the intersection point is most close to P1, then we say that this ray hits on the surface (P1, P2, P3). After the reflective facet is classified, we calculate the intersection point and the vector of the reflective ray.

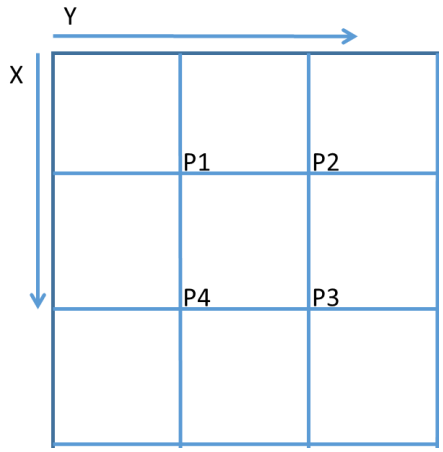


Figure 32. A top view of the 3-D random surface.

The images of the pipe with a random rough surface are shown in Figure 33. The Matlab simulation of a 1x1x30 mm light pipe with one rough surface is shown in Figure 34, and comparison between Matlab and Zemax is shown in Figure 35. As the conclusion gotten from 2-D simulation, m value is the most critical indicator of the average scattering loss rather than roughness.

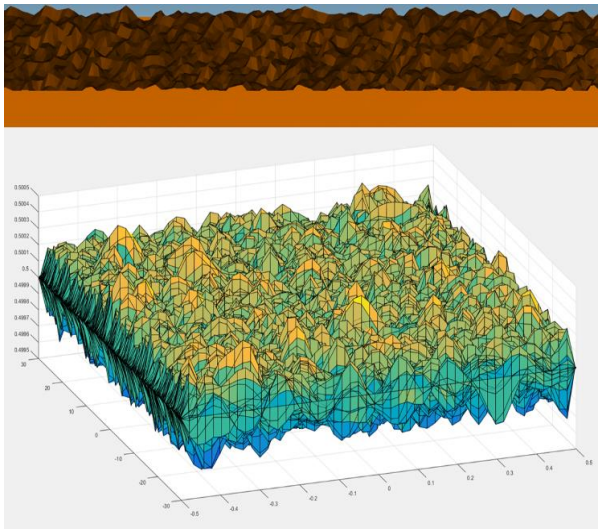

Figure 33. The 3-D random surface created by Zemax (up) and Matlab (down).

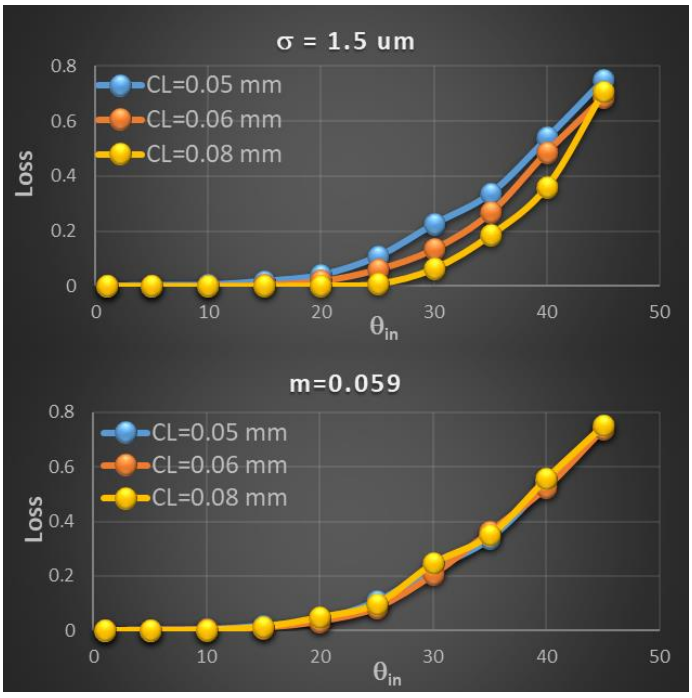


Figure 34. The 3-D scattering loss simulation by Matlab. Here CL is the correlation length.

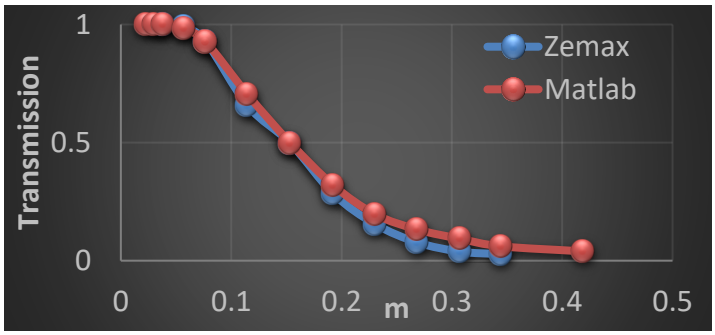


Figure 35. Comparison between Matlab and Zemax as $\theta_{in}$ = 5°.

Simulating the scattering loss by using Matlab, Zemax or TracePro has different advantages. For example, Matlab provides the maximum freedom to create an arbitrary surface, Zemax can load an object made by Matlab and provide a reliable ray tracing result, and TracePro can create a periodic surface easily. On the reverse side, Matlab does not have the ray tracing code in its library, Zemax cannot quickly revise the object with a random surface, and TracePro cannot create an object with the random surface. Hence, in our application, Matlab is the most convenient software to simulate the scattering light in various conditions, and we verify this simulation result through using Zemax and TracPro.

3.5 Comparison between the random and periodic surface

Figure 36 shows a comparison of scattering loss between 3-D periodic and random surface simulated by TracePro and Zemax, respectively. As Figure 27, Figure 36 also shows a perfect agreement between periodic and random surface, and the testing conditions are: $\theta_{in} = 45°$, length = 30 mm, height = width = 1 mm, and radias of source = 0.2 mm. Based on all of the evidence shown in Figure 27 and Figure 36, it seems it is unnecessary to create a random surface to simulate the scattering light. Nevertheless, it is frequently to get into a specific situation that cannot correctly represent the scattering behavior of the whole light pipe. For example, the ray may always

hit on the wave crest or trough when it propagates inside of a pipe with a sinusoidal surface (see Figure 38(a)), or a ray that violates the TIR is refracted back into the pipe (see Figure 38(b)). It is not wrong, but this result cannot represent the average scattering behavior of a random surface that has the same RMS slope with the periodic surface. The red line in Figure 37 is the same as the red line in Figure 36. Hence, it is obvious the curve with 0° divergence angle (blue line) is not a proper simulation. To solve this problem, we may increase the complexity of the simulation, e.g., increase the divergence angle of the source or chose a polyhedron to be the unit tile. However, it is always hard to say if the current setup is proper to represent the average scattering behavior.

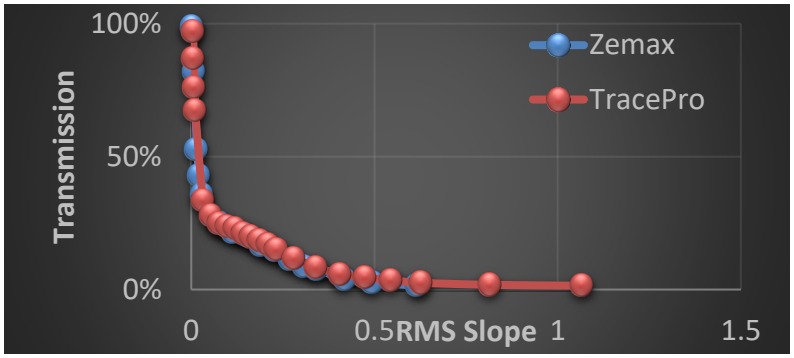


Figure 36. The random surface and periodic surface (sphere tile) are simulated by Zemax and TracePro, respectively. The divergence angle of the source in TracePro is 0.01°.

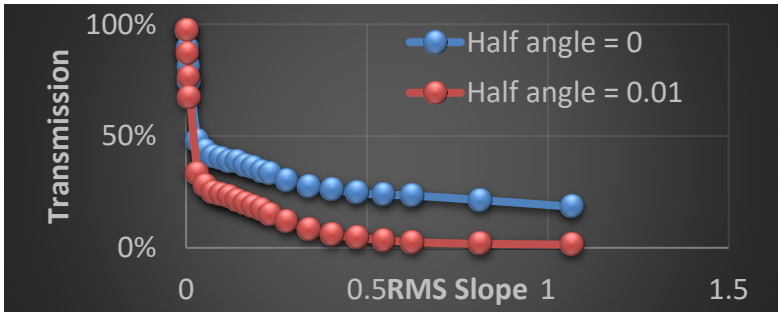


Figure 37. Scattering simulation base on different divergence angle, 0° and 0.01°, where the shape of the tile is a sphere.

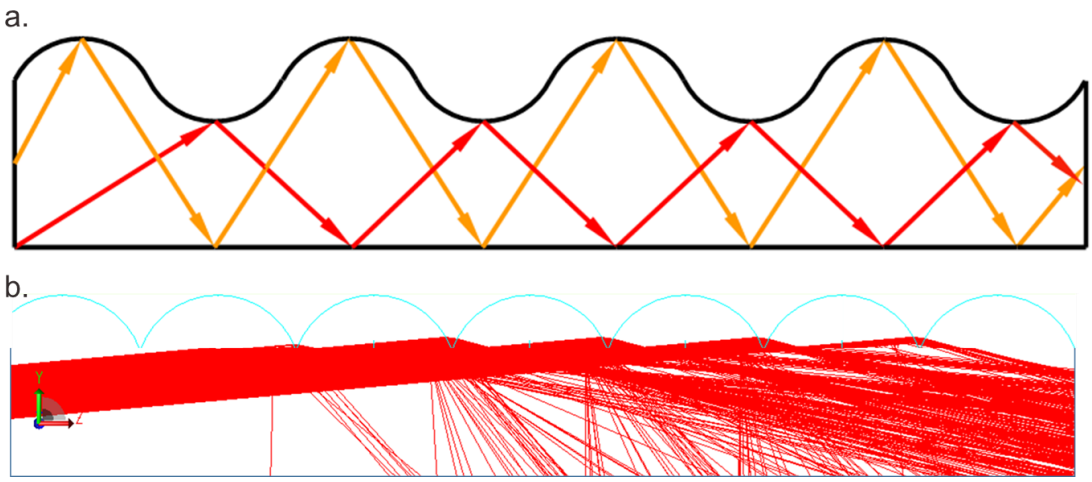


Figure 38. A light pipe with a periodic surface.

There is another comparison shown in Figure 39. In Figure 39 (a), the transmittance fluctuates with the spatial wavelength (Λ) intensely as the half angle of the source is 0°, but the trend is relatively stable as the half angle is 0.2°. However, Figure 39 (b) shows that the trend of the transmittance is stable for both two case, L= 75 mm and 150 mm, as the half angle is 0°. The reason is that the shape of the tile used in (b) is a sphere, and the sphere tile provides more possibility of the reflective direction than a pyramid. In (b), the blue line is a pipe has two rough surfaces (up and down) as the length is 75 mm, and the orange line has one rough surface as the length is 150 mm. Another essential information shown in this graph is that average loss of a pipe has one rough surface and double length is equal to the pipe has two rough surfaces and half length.

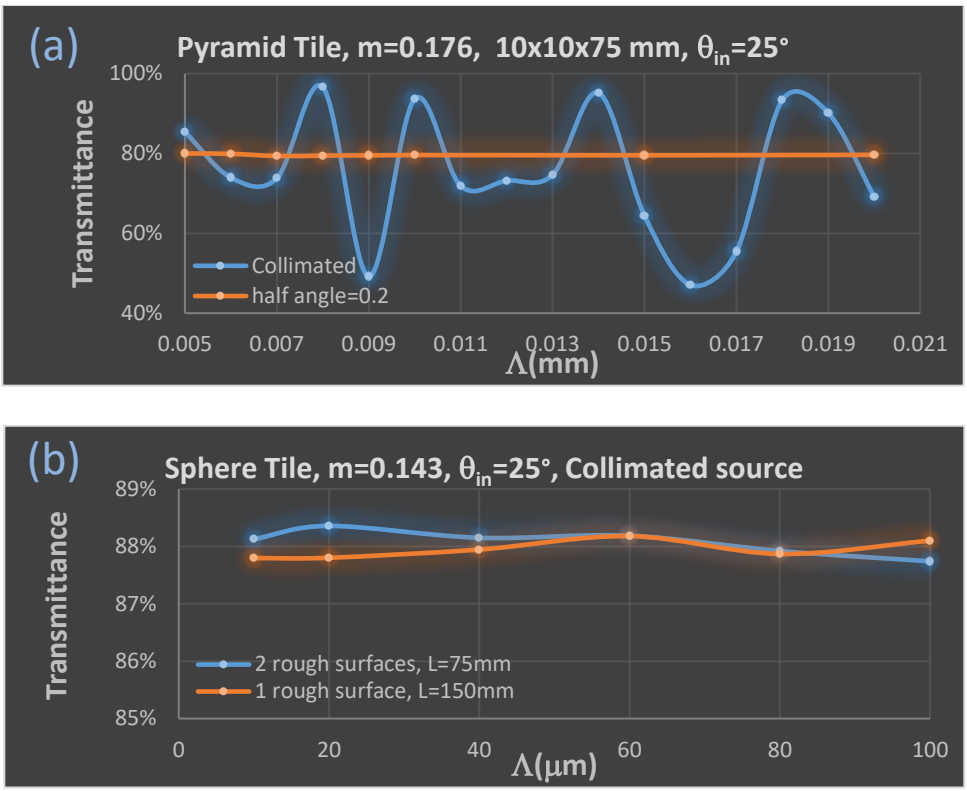


Figure 39. (a) A comparison of transmittance as the half angle is 0° and 0.2°, m = 0.176, and $\theta_{in}$ = 25° for a 10X10X75 mm light pipe with a pyramid surface. (b) A comparison of transmittance as $\theta_{in}$ = 0°, m = 0.143, length of pipe is 75 mm and 150 mm.

## 3.6 Experiment

### 3.6.1 Sample preparation

Since the material of these two samples is both fused silica and the required dimension is relatively small, e.g., 1x1x50 mm, the traditional laser cutting technique is not appropriate. The traditional laser cutting technique, e.g., $CO_2$ laser and Nd:YAG lasers, cuts the sample through focusing the laser beam on the sample surface and then melts the edge. The primary mechanism is the absorption and band gap energy of the material, i.e., it only works as the material can absorb the wavelength of the laser. However, the transmittance of the fused silica is almost 100% from

200 nm to 2000 nm [30]. Furthermore, the extra heat will melt or bend the edge of the sample, especially as the dimension is small.

The femtosecond laser the fastest laser in the world, and it can be applied to almost any material. The pulse period is around $10^{-15}$ second, and this period is shorter than the electron-phonon time of the material. Hence, the effect of heat conduction can be ignored, i.e., the femtosecond laser will not bend the cutting edge. Another characteristic of the femtosecond laser is ultrahigh power density. For example, if the energy of the laser is 1 mJ, the pulse period is 100fs, and the diameter of the focal point is 20 μm, then the power density will be around $10^{15}$ W/cm$^2$. This such high power density causes the nonlinear multi-photon absorption as the laser interacts with the material, and this characteristic makes the femtosecond laser can be employed without considering transmittance and band gap of the material.

The samples used in this section was produced by a technique names Femtosecond Laser Irradiation and Chemical Etching (FLICE). FLICE is a common microfabrication technology to fabricate the microfluidic channels or waveguide. It includes two steps [31]:

Step 1: Irradiate the femtosecond laser on the substrate with the intensities lower than the laser ablation threshold (see Figure 40).

Step 2: Etch the modified region by using HF acid.

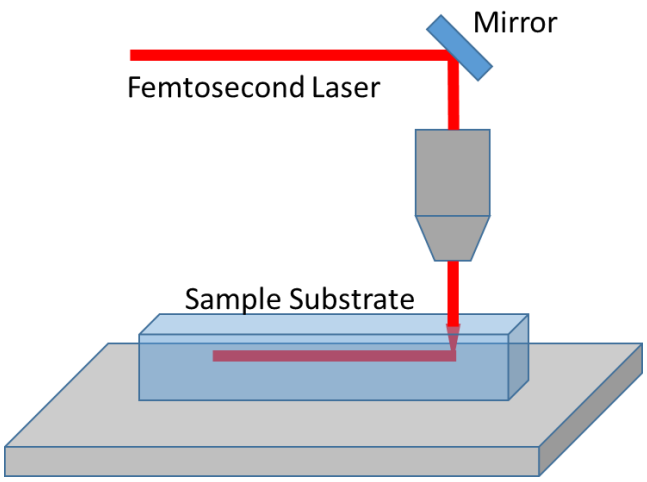


Figure 40. Using the femtosecond laser to cut the fused silica.

### 3.6.2 Measurement

In this section, we will measure the scattering loss as the incident angle is from 0° to 60° for two different samples, and compare the measurement data with the geometric optics simulation. The setup of the measurement is shown in Figure 41, and it includes a laser, a beam splitter, a fiber, a rotation stage, and two detectors. Here, we use a supercontinuum white light laser (450-2400 nm) from NKT Photonics (SuperK COMPACT [32]), and use a filter to select the desired incident wavelength. After the light pass through the beam splitter, it will be collected by two Integrating Sphere Photodiode Power Sensors (S142C from Thorlabs), and then read by a power meter (PM320E from Thorlab). Although the maximum power of the supercontinuum laser happen as the wavelength is 1100 nm, it is not the best working range for the power sensor. Hence, we select 514 nm as our input wavelength. For guaranteeing all of the output light can be collected by the detector 1, we insert the output aperture into the detector.

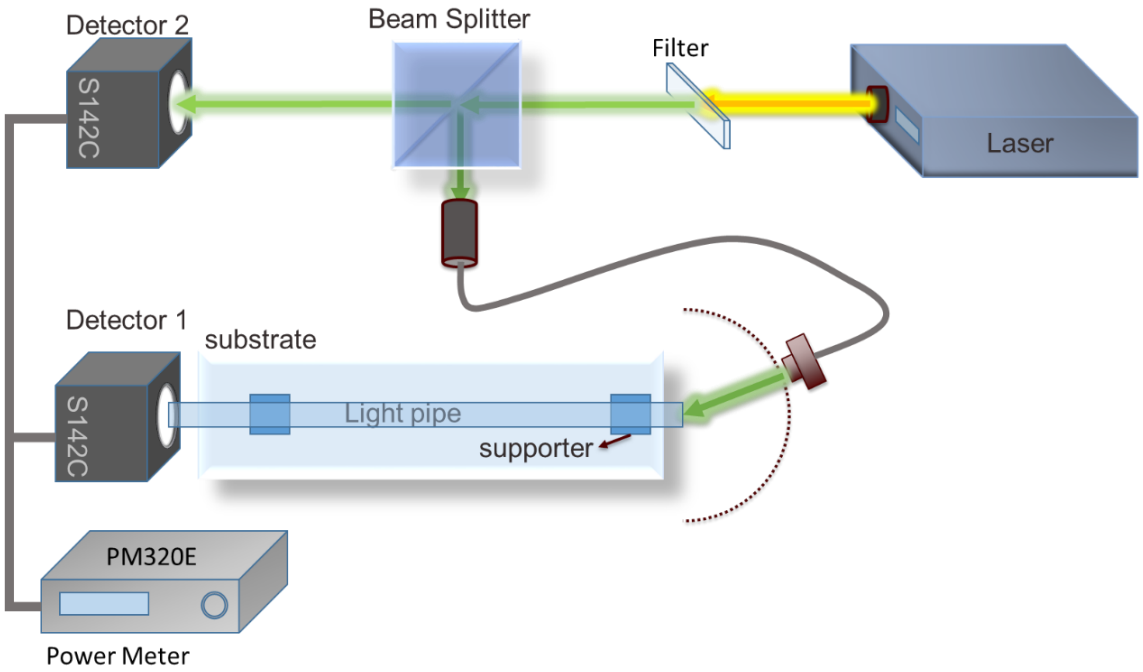


Figure 41. The setup of scattering measurement. The rotation center is at the input facet of the sample.

Before starting the measurement, we need to check the stability of power of the laser. The first step is to record the power for twenty minutes for both two detectors without a sample (see Figure 42 (a) and (b)), and divide the power of detector 1 by the power of detector 2 (see Figure 42 (c)). As shown in Figure 42, the coefficient of variation of the power is 1% for both two detectors, but it can be reduced to 0.21% by taking the ratio between two detectors. Hence, we only record the power ratio as measuring the transmittance of the sample. The steps of measurement are:

1) Record the power ratio for ten seconds without a sample, work out the average, and assume this value is 100% of transmittance.
2) Record the power ratio for ten seconds with a sample, work out the average, and calculate the transmittance by dividing this value by the average ratio get from step one.

3) Rotate the fiber and repeat step one and two.

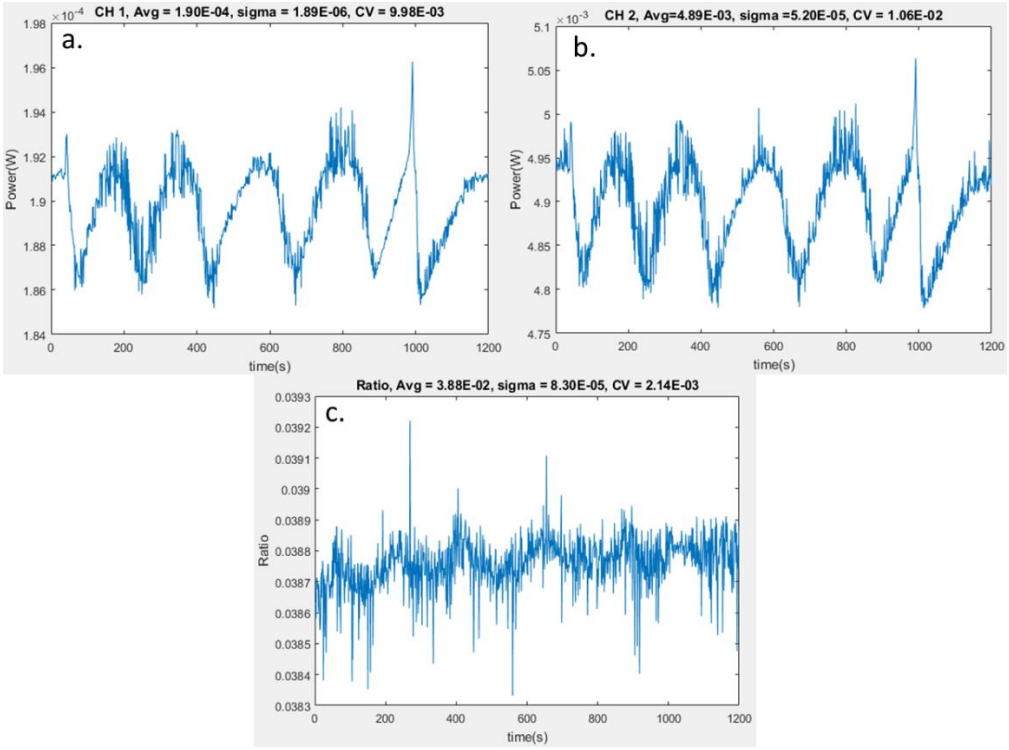


Figure 42. Figure (a) and (b) are the power of detector 1 and detector 2, respectively. Figure (c) is the power ration between two detectors.

The structure of sample 1 is shown in Figure 43. For reducing the possible factors which can cause extra loss, we mount the light pipe on two small supporters to make sure this sample is surrounded by air, and stick the coverslip on both input and output facet. The four side walls in the X and Y direction are polished cut surface, and the other two side walls in Z direction are the original surface. We use a light source with beam size = 0.34 mm, divergence angle = 12°, and $\lambda = 514$ nm, and scan the sample on XY plane from 0° to 55°. The measurement result is shown in Figure 44 (blue line).

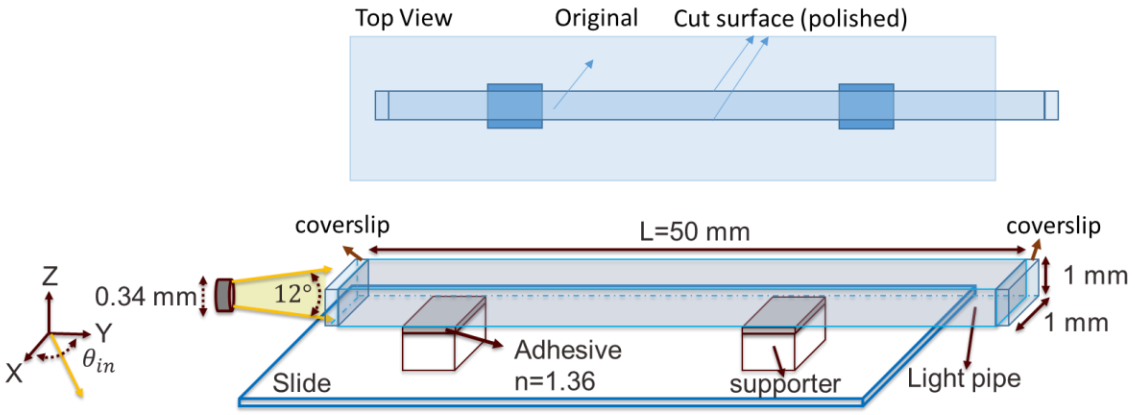


Figure 43. Sample 1: 1x1x50 mm, fused silica, with two polished side wall in X an Y direction.

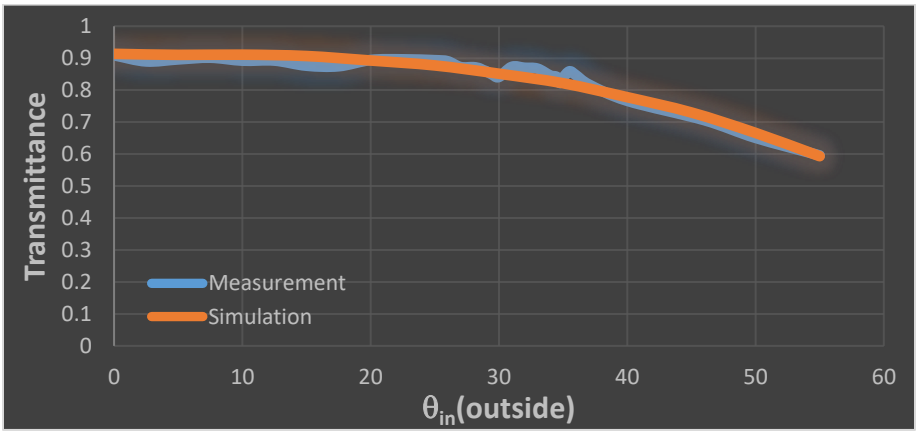


Figure 44. Comparison of transmittance between measurement and simulation. The blue line is the measurement data, and the orange line is the simulation data of TracePro as $m_{side}$ = 0.038 for two side wall.

Next, we simulate the scattering loss base on the same conditions with the measurement through using TracePro and follow three rules to find the suitable RMS slope. The rules are:

- RMS slope of the input and output surface ($m_{side}$) affect the transmittance as $\theta_{in} = 0°$.
- RMS slope of the sidewall ($m_{in\&out}$) affects the roll-off point of the transmittance vs. $\theta_{in}$ curve.
- Beam size affects the slope of the curve after the roll-off point as the beam partially hit on the sidewall.

These three rules are not entirely independent of each other. For example, if $m_{side}$ is too small, e.g., < 0.04, then $m_{in\&out}$ is hard to affect the transmittance. Hence, a better start is to find a suitable $m_{side}$ to match the transmittance of a large $\theta_{in}$, e.g., 55°, and then adjust this value to fit the measurment data. In this case, we found $m_{side}$ = 0.038 (see the orange line in Figure 44). We utilize two coverslips to alleviate the effect caused by the roughness of input and output facet; we expect we can ignore $m_{in\&out}$. Indeed, the transmittance of measurement (90.9%) and simulation (91.3%) are almost the same as $m_{in\&out} = 0$ and $\theta_{in} = 0°$ (see the orange line in Figure 44). This case is relatively simple because we got an excellent agreement between simulation and measurement by contronlling only one variable ($m_{side}$). This implys that the quality of this sample is fine, therefore the only factor which causes loss is $m_{side}$.

The structure of sample 2 is shown in Figure 45. For reducing the extra loss from the adhesive layer, we split the supporters from two to four to reduce the contact area. Furthermore, for investigating the impact of $m_{in\&out}$ on the transmittance, we do not use the coverslip to reduce the scattering loss on both input and output facet. The four side walls in the X and Y direction are polished cut surface, and the other two side walls in Z direction are the original surface. We use a light source with beam size = 0.54 mm, divergence angle = 0.3°, and λ=514 nm, and scan the sample on XY plane form 0° to 60°. The measurement result is shown in Figure 46 (blue line).

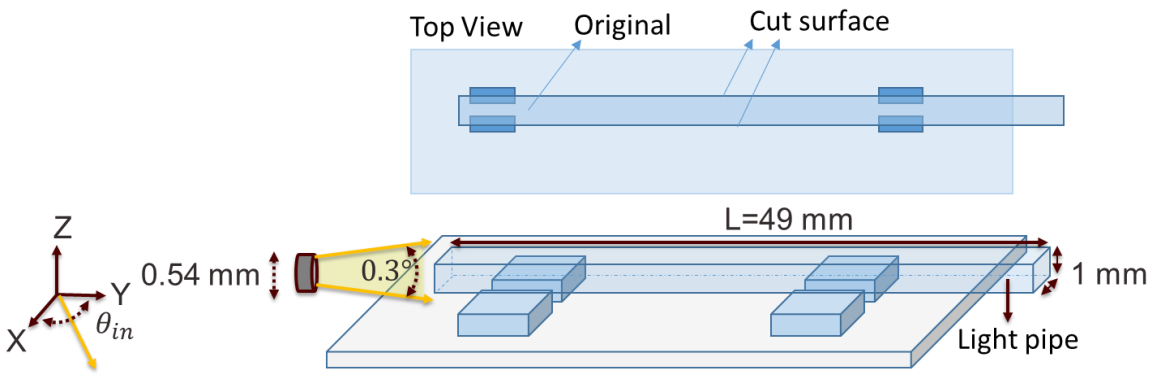


Figure 45. Sample2: 1x1x49 mm, fused silica, with two polished side wall in X and Y direction.

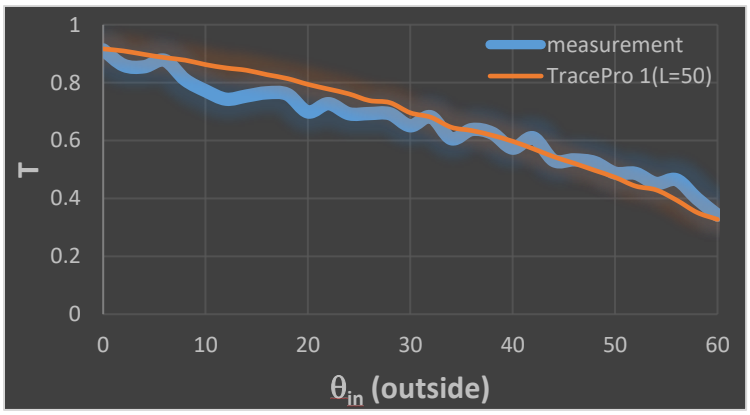


Figure 46. Comparison of transmittance between measurement and simulation. The blue line is the measurement data, and the orange line is the simulation data of TracePro as $m_{side}$ = 0.1425 and $m_{in\&out}$ = 0.0653.

Follow the simulation process that we did in case 1, and we found a good agreement between measurement and simulation as $m_{side}$ = 0.1425 and $m_{in\&out}$ = 0.0653. Some slight ripples can be observed from both measurement and simulation, and it is mainly caused by $m_{side}$. If $m_{side}$ is larger, then the ripples become larger. Compare with case 1, the difference between measurement and simulation, and the fluctuation are relatively larger. It implies two things. First, a larger fluctuation means larger RMS slope and worse quality of the surface. Second, larger error

implies that the surface scattering is not the only reason to cause loss, i.e., we have to consider bulk scattering in this case to get a better agreement, and we indeed observe some air bubbles and crack inside this sample. Nevertheless, the distribution of these bubbles and crack is not uniform, and therefore it is hard to simulate the bulk scattering and the loss caused by the crack. Another indicator which can represent the surface quality is the roll-off point of the transmittance. The transmittance of a light pipe with the perfect surface (the roughness can be ignored) drops immediately to zero as the incident angle equal to the critical angle; it means that if the roll-off point is closer to the critical angle, then the quality of the surface will be better. Base on this concept, sample 1 should have a smoother surface compared to sample 2. Indeed, the m value of sample 1 is much smaller than the m value of sample 2.

Restricted by our current technic, we have not gotten an accurate surface profile, yet. The maximum scale of our surface profile measurement is 90 μm X 90 μm; it is much smaller than our sample. Another issue is that the measurement relies on the reflection light from the target surface, but the edge of the sample is always round. The round edge increases the uncertainty and decreases the precision. Hence, we did not compare m value between simulation and measurement, but we proved that the scattering loss is indeed dominated by the RMS slope by comparing the transmittance of simulation and measurement.

### 3.7 Comparison of geometric and physical optics approximation (ABg)

Actually, the conclusion about the RMS slope gotten from the previous subsections is not surprised because all of the simulations are analyzed based on geometric optics (GO) approximation. We also proved that surface scattering loss of the light pipe could be simulated by only considering the RMS slope of the surface. In this section, we will compare the simulation

result between GO approximation and ABg to see if the GO approximation can be replaced by ABg.

ABg model is one of the most familiar scattering models can be used in the optical software, and it is usually written as

$$\text{BSDF} = \frac{A}{B+(\beta-\beta_0)^g},$$

where $\beta = \sin\theta_{scatter}, \beta_0 = \sin\theta_{specular}$, and A, B and g are the parameters of the model. To get a correct simulation by using ABg model we have to follow these rules [33]:

- Isotropic surface roughness.
- Surface roughness must be much less than the wavelength of the incident light.
- The spatial frequencies of the surface roughness must be bandwidth-limited.

First, we build a 2-D light pipe with the testing conditions as $\theta_{in} = 40°, n_{cl} = 1, n_{co} = 1.4, m = 0.0141, and\ W = 1\ mm$ in Matlab, and simulate the scattering loss as what we did in the section 3.3 (see the blue line in Figure 47 ). Next, simulate the scattering loss base ob the same condition by using Zemax. The function that Zemax calculates the scattering loss by using ABg model is:

$$\text{Loss} = 1 - (1 - TIS)^{interscetions},$$

where TIS (Total integrated scatter) is:

$$TIS = \frac{diffuse\ reflectance}{total\ reflectance}.$$

If TIS = [0.043 0.0093], then loss calculated by ABg will equal to the loss of GO approximation as length =[20 400] mm, and pick a middle value for TIS between 0.043 and 0.0093 to be another comparison. Based on the given $\theta_{in}$, W, and L, the intersection number and total scattering loss can be easily worked out without using Zemax, and then compare this result with the GO approximation. As the result shown in Figure 47, the curves of scattering loss simulate by ABg

(orange, yellow, and gray line) are entirely different with GO approximation (blue line) no matter what the value of TIS is.

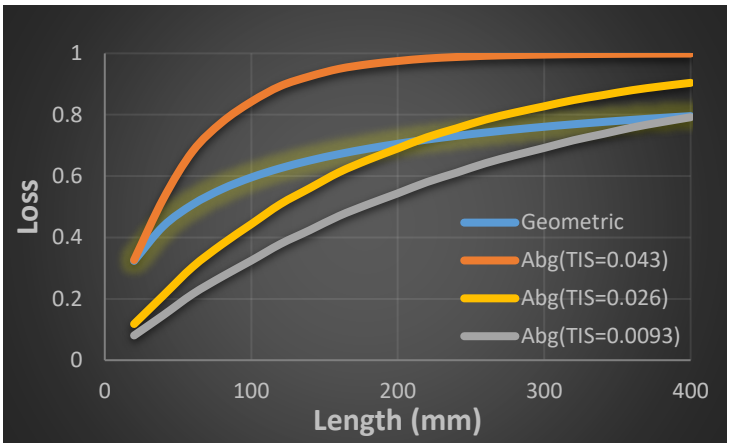


Figure 47. The testing conditions are $\theta_{in} = 40°$, $n_{cl} = 1$, $n_{co} = 1.4$, and W = 1 mm, where $\theta_{in}$ is inside of the pipe, $n_{cl}$ and $n_{co}$ are the refractive index for cladding layer and core layer, respectively, and W is the width of the pipe. The light pipe only has two rough surface.

In the previous example, we did not exactly use the ABg model; we assumed three different values of TIS and compared the loss with GO approximation base on the given RMS slope. Now, we want to work out the RMS slope, RMS roughness, and correlation length by the given A, B, and g. First, we assume a set of value for A, B, and g, [A B g] = [0.0005 0.001 2], and calculate the corresponding BRDF. By using the Rayleigh-Rice equation [34], the power spectral density (PSD) can be calculated from BRDF. The equation is written as:

$$PSD(f_x) = \frac{\lambda^3 \times BRDF}{16 \times \pi^2 \times \cos\theta_i \times \cos\theta_s \times Q} \ \mu m^3$$

and

$$f_x = \frac{\sin\theta_s - \sin\theta_i}{\lambda},$$

where $\theta_s$ and $\theta_i$ is the scattering angle and incident angle, respectively, and Q is a dimensionless reflectivity polarization factor. For some special case, e.g., a s-polarization source or high-reflectance surface, Q are nearly one [34, 35], nevertheless, that are not our case. For an unpolarized source, the functions of Q are written as [34]:

$$\mathrm{Q} = \frac{1}{2}\sum_{\alpha}\sum_{\beta} Q_{\alpha\beta}$$

$$Q_{ss} = \left|\frac{(\varepsilon-1)\sqrt{\varepsilon - sin^2\theta_s}\cos\Phi_s}{(\cos\theta_i + \sqrt{\varepsilon - sin^2\theta_i})(\cos\theta_s + \sqrt{\varepsilon - sin^2\theta_s})}\right|^2$$

$$Q_{sp} = \left|\frac{(\varepsilon-1)\sqrt{\varepsilon - sin^2\theta_s}\sin\Phi_s}{(\cos\theta_i + \sqrt{\varepsilon - sin^2\theta_i})(\varepsilon\cos\theta_s + \sqrt{\varepsilon - sin^2\theta_s})}\right|^2$$

$$Q_{ps} = \left|\frac{(\varepsilon-1)\sqrt{\varepsilon - sin^2\theta_i}\sin\Phi_s}{(\varepsilon\cos\theta_i + \sqrt{\varepsilon - sin^2\theta_i})(\cos\theta_s + \sqrt{\varepsilon - sin^2\theta_s})}\right|^2$$

$$Q_{pp} = \left|\frac{(\varepsilon-1)(\sqrt{\varepsilon - sin^2\theta_s}\sqrt{\varepsilon - sin^2\theta_i}\cos\Phi_s - \varepsilon\sin\theta_i\sin\theta_s)}{(\varepsilon\cos\theta_i + \sqrt{\varepsilon - sin^2\theta_i})(\varepsilon\cos\theta_s + \sqrt{\varepsilon - sin^2\theta_s})}\right|^2$$

Here, $\alpha$ and $\beta$ are either s-polarization or p-polarization, $\theta_{in}$ is the incident angle, $\theta_s$ is the scattering angle, and $\phi_s$ is the scattering angle on the reflection surface. Since we are considering a 2-D case, we assume $\phi_s$ is zero. In the above equations, $\varepsilon$ is the relative dielectric constant equal to $\varepsilon_{incident}/\varepsilon_{refraction}$. For example, if we consider the reflective scattering behavior at an air-material interface and assume the dielectric constant of air is one, then $\varepsilon = \varepsilon_{refraction}$ for scattering on the air side, and $\varepsilon = 1/\varepsilon_{incident}$ for scattering on the material side. The RMS roughness ($\sigma$), RMS slope (m), and correlation length ($\ell_c$) can be calculated by:

$$\sigma^2 = 2 \times \sum_{k=k_{min}}^{k=k_{max}} PSD(f_k) \times \Delta f_k,$$

$$m^2 = 2 \times \sum_{k=}^{k=k_{max}} (2\pi \times f_k)^2 PSD(f_k) \times \Delta f_k,$$

and

$$\ell_c = \sqrt{2}\frac{\sigma}{m}.$$

After we get the $\sigma$, m, and $\ell_c$ by the given [A B g], we can run the GO approximation and compare it with ABg model. Here, σ = 0.01 μm, m = 0.019, and $\ell_c$ = 0.752 μm. As the result shown in Figure 48, the difference between these two models is getting larger as the length of the pipe is getting longer. It is not surprised these two models cannot agree with each other, because one of them is based on physical optics and another one is based on geometric optics. However, a problem emerges here is that if the sample does not satisfy the requirements of the ABg model or Rayleigh smooth-surface criterion, then it will be difficult to simulate the scattering behavior in Zemax without BRDF.

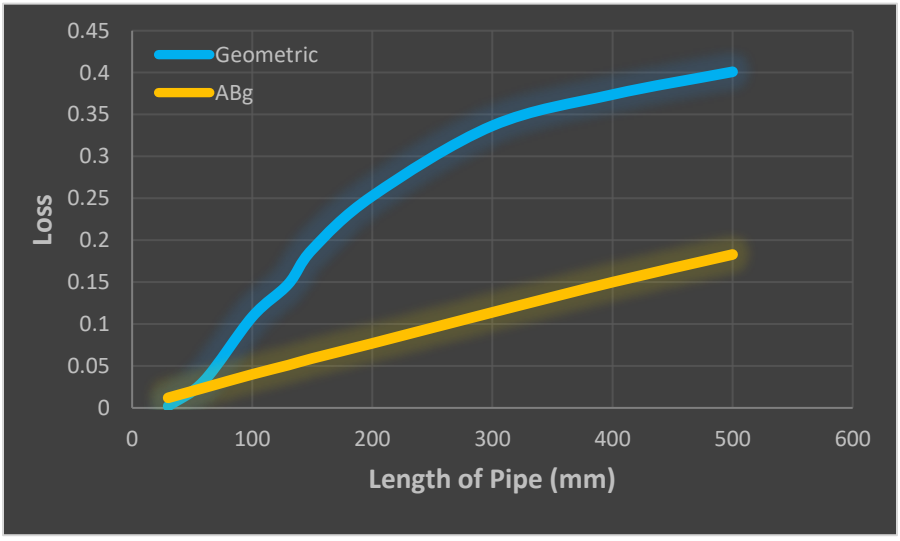


Figure 48. A comparison between GO approximation and ABg model as $\theta_{in}$ = 70°, $n_{cl}$ = 1, $n_{co}$ = 1.49, and the height of pipe is 1 mm.

## 3.8 Data fitting (2-D)

The whole process of the scattering loss simulation is somewhat time-consuming because we trace one ray per time, and for getting a highly accurate result, we need to run the simulation 3000 times in every different condition. Therefore, we want to find an efficient method to decrease the simulation time. One of the ways is to find some fitting equations that can represent the statistic simulation result.

Figure 49 shows the plot of the scattering loss versus RMS slope for incident angle ($\theta_{in}$) from 1° to 45°, then we use the function

$$\mathrm{Y} = 1 - \frac{1}{1 + \left(\frac{x}{x_0}\right)^p}$$

to fit each curve, as shown in Figure 50. The function, Y(x, $x_0$, p), comes from a "logistic model" applicable to exponential growth having a bounded nature. For our application, Y is la oss from zero to one, x is the RMS slope of the surface, $x_0$ is a midpoint value when Y = 0.5, and p controls the slope of the curve. Let's rewrite this equation as

$$\mathrm{Loss} = 1 - \frac{1}{1+\left(\frac{m}{m_0}\right)^p}.$$

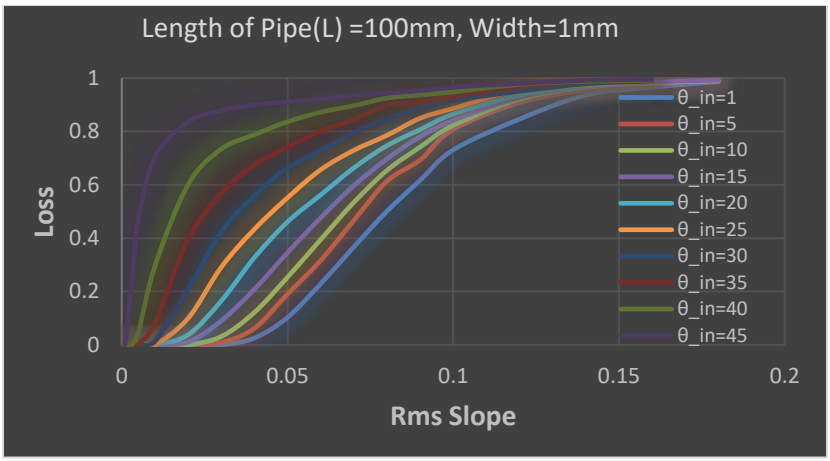


Figure 49. $\theta_{in}$ means the angle between the ray and the optical propagation axis inside of the pipe.

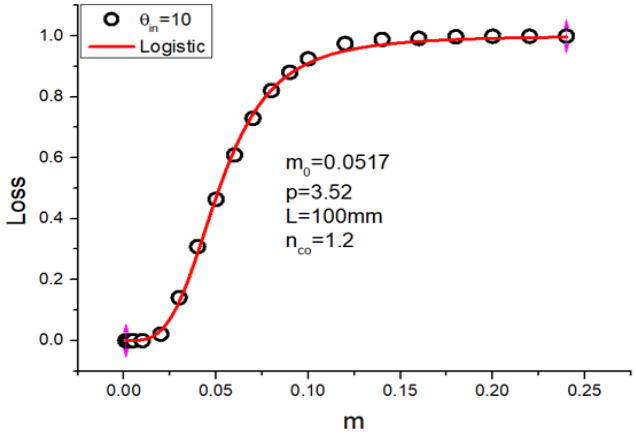


Figure 50. Parameters: L=100 mm, $n_{cl}/n_{co}$=1/1.49, width=1 mm.

After repeating the previous fitting process for different length (L), we get two graphs, p versus $\theta_{in}$ (see Figure 51) and $m_0$ versus $\theta_{in}$. Figure 51 shows p is independent of the length of pipe, L, for the given $n_{co}$ and $n_{cl}$, and then we combine the $\theta_{in}$ with $\theta_c$ as $(\theta_c-\theta_{in})/\theta_c$, as shown in Figure 52. Now, p is the function of $\theta_c-\theta_{in})/\theta_c$, after fitting it by a linear equation we get

$$P = 3.5547 \times \frac{\theta_c-\theta_{in}}{\theta_c} + 0.9349,$$

where $\theta_c$ is the complementary angle of the critical angle as written by

$$\theta_c = 90° - \sin^{-1}(\frac{n_{cl}}{n_{co}}).$$

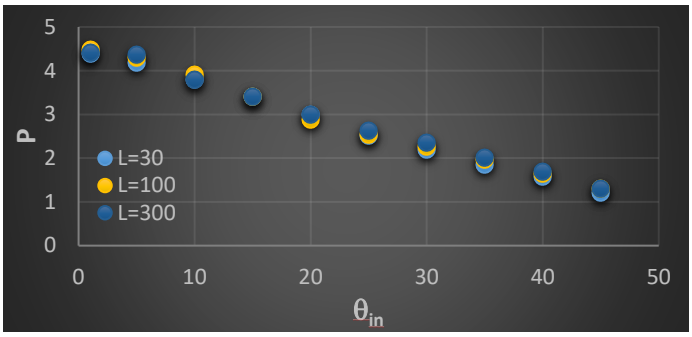


Figure 51. The plot of p versus $\theta_{in}$ for different length as $n_{cl}$=1 and $n_{co}$=1.49.

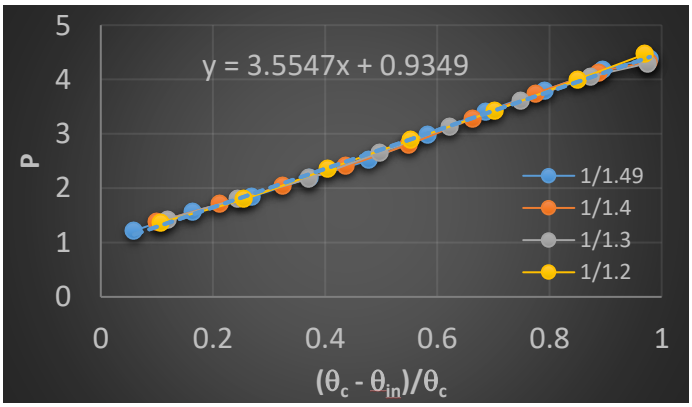


Figure 52. Here, $\boldsymbol{\theta_c = 90 - \sin^{-1}(\frac{n_{cl}}{n_{co}})}$.

After fitting the curve shown in Figure 53 by the quadratic equation

$$m_0 = -a \times \left(\frac{\theta_c - \theta_{in}}{\theta_c}\right)^2 + b \times \frac{\theta_c - \theta_{in}}{\theta_c} + c$$

we found: 1. The first coefficient, "a," is a constant when L is fixed. 2. The constant term, "c," should be zero in term of the definition of $m_0$. Repeating this process for different L, and find all

corresponding value of “a” and “b.” The fitting results for coefficient a, b, and d are shown in Figure 54, and the equations are written as

$$a = 1.116 \times \left(\frac{L}{W}\right)^{-0.755},$$

$$b = d \times \left(\frac{L}{W}\right)^{-0.55},$$

and

$$d = -0.965\frac{\theta_c}{90°}^{2} + \frac{\theta_c}{90°}1.8596 + 0.6875.$$

The deviation of the scattering loss calculated by these equations and Matlab is lower than 3 %, as sown in Figure 55.

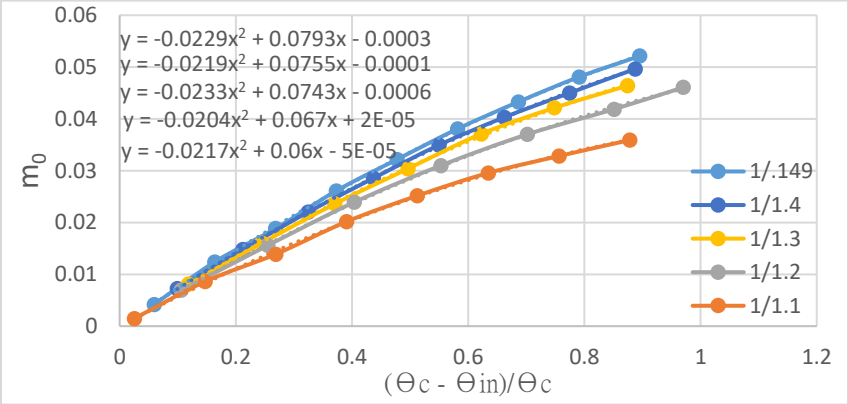


Figure 53. A plot of $m_0$ versus $(\theta_c-\theta_{in})/\theta_c$ as L= 200 mm.

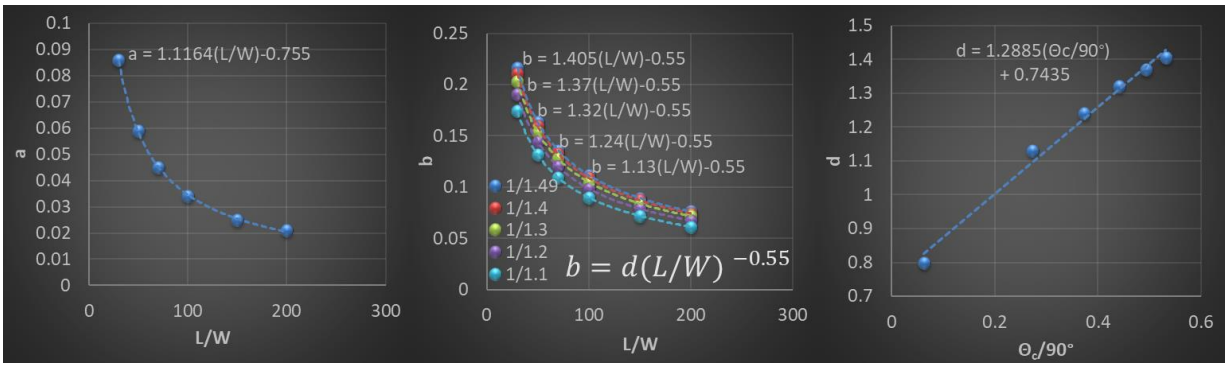


Figure 54. Relate the coefficient "a "and "b" to L/W, where W is the thickness of pipe.

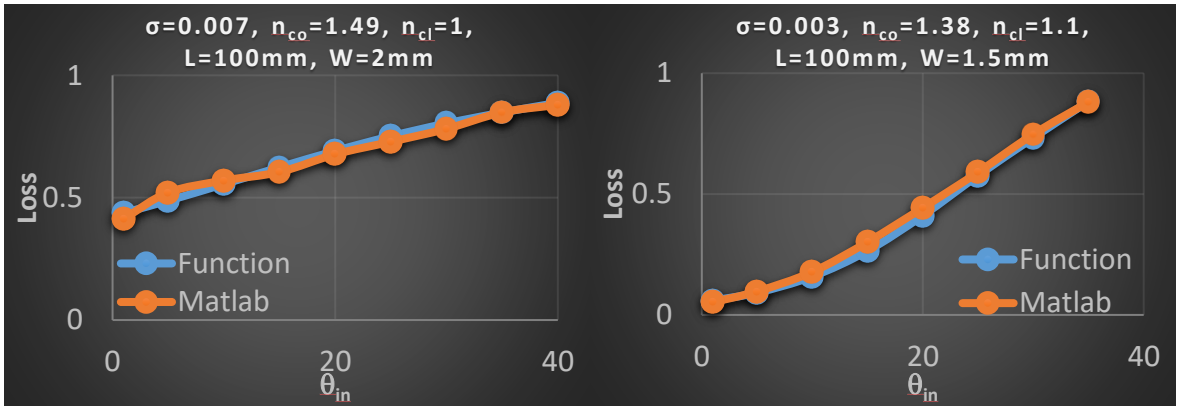


Figure 55. Comparison of scattering loss between Matlab simulation and our equations as two different testing conditions.

## 3.9 Summary

For predicting the outcoupling loss for an unknown sample without doing BSDF, we need a more reliable indicator to describe loss mechanism for a light pipe. From the simulation results in this section, no matter the surface is periodic or random, if they have the same RMS slope, then they will have the same outcoupling loss. To be more precise, the GO approximation is based on the Snell's law and TIR, and both these two theories consider the local angle of every facet.

Therefore, it is not sufficient to only consider the RMS height. We also proved that the scattering behavior between periodic and random surface could be the same, but the periodic surface will cause more uncertainties. By comparing the GO approximation with measurement data and ABg model, we found the GO approximation has an excellent agreement with the measurement, and GO approximation cannot be replaced by ABg. Base on the 2-D and 3-D simulation, we believe RMS slope is a more general predictor of outcoupling loss, and it can be applied to the arbitrary surface.

# 4. TRADE-OFF OF THE CONCENTRATOR DESIGN

Although our new design solves the issues in Liu's design, there still exist some weakness in our design. For example, this design highly requests on the quality of HR coating and polish. Furthermore, we also wonder if it is possible to achieve a higher concentration based on the current structure. Several possible designs that may improve the performance of this system were proposed and discussed in this section.

## 4.1 Beam expander

The minimum incident angle on the $45°$ surface of the coupler is $28°$, and the critical angle is around $42.5°$ on the interface between air and fused silica (see Figure 56). The loss due to the violation of TIR is 37.7% (without HRC), and 3.8% with HRC. The total intersections inside the pipe can be calculated by

$$Intersections = 1 + \frac{L \times \tan\theta}{W},$$

where L is the length of pipe, W is the width, and $\theta$ is the angle between ray and ground. Assuming L/W =100, then the intersections are 31 as $\theta = 17°$.

Apparently, for alleviating the demands of the quality of HR coding and surface polish, it is necessary to decrease the incident angle inside of the coupler. Hence, we designed an aspherical concave lens and mounted it on the top of the coupler, as shown in Figure 56. This concept is like a beam expander, but inverse direction. The distance between the first lens and the concave lens is equal to the summation of the focal length of two lenses, $f_1 + f_2$, here, $f_2 < 0$ (see Figure 58). Because the beam expander parallels the rays, the total interactions inside of the waveguide are considerably reduced. Therefore, the tolerance of surface roughness on waveguide could be larger. After

employing the concave lens, the loss on the 45° surface is decreased to 1% (without HRC), the intersections are 7, and the divergence angle is ±4° (see Figure 59) compare to ±17°.

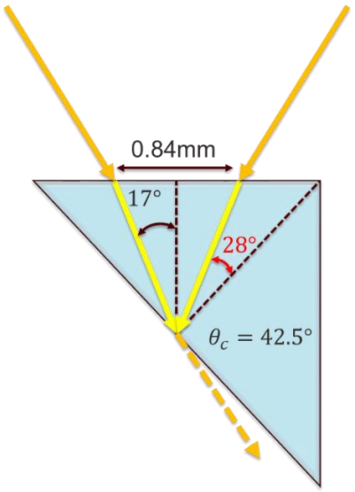


Figure 56. The incident light hit on the prism coupler.

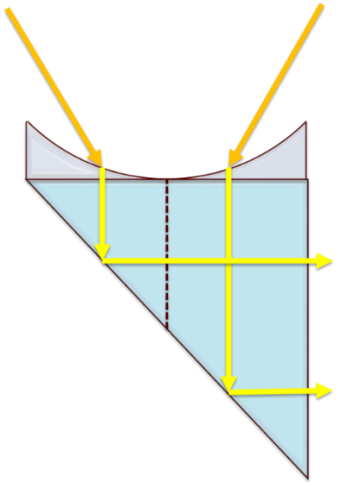

Figure 57. Install a concave lens on the prism coupler.

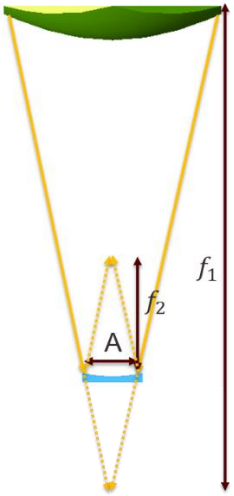


Figure 58. The distance between two lenses, and $f_1$ and $f_2$ is the focal length of the green lens and blue lens as $\lambda$= 1.8 μm, respectively.

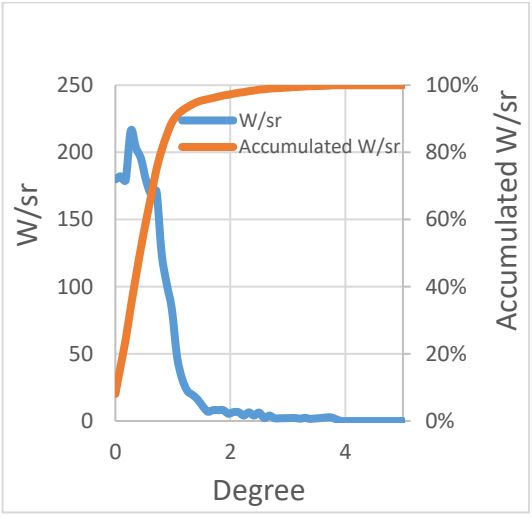


Figure 59. The graph of angular distribution after the concave lens, and the maximum accumulated power is 100% as θ = 4°.

## 4.2 Linear concentrator (LC)

The loss caused by an imperfect HR coating and roughness of the surface is improved by adding a concave lens. The next step is to verify if this design causes any new issue and increase the total concentration of this system. The linear concentrator is the most straightforward non-imaging concentrator. It is composed of four trapezoids without any curved surface and can be easily fabricated with lower cost. Hence, LC is a preferable option of the second concentrator in the CPV system. The basic shape of the LC is shown in Figure 60. The light propagates inside the concentrator through TIR.

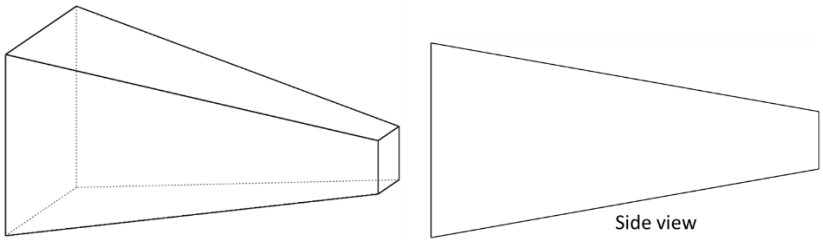


Figure 60. A basic schematic of a linear concentrator.

The light travels inside the LC can be viewed as shown in Figure 61 (a). The colorful solid lines and dotted line are the real propagation path and imagined path, respectively. For finding the minimum length (L) of the LC by given a critical angle ($\theta_c$), input aperture (A), tapered angle (θ), and incident angle ($\theta_{in}$), we can use the following equations:

$$R = \frac{A_1}{\tan\theta},$$

$$N = \left\lfloor \frac{(90° - \theta_c - \theta_{in} - 2\theta)}{2\theta} \right\rfloor,$$

$$\ell_1 = \frac{2A_1}{\tan\theta + \tan(\theta_{in} + 2\theta)},$$

$$\ell_n = \frac{2\tan\times(R-\sum_{k=1}^{k=n-1}\ell_k)}{\tan\theta+\tan(\theta_{in}+(n+1)\theta)},\ \mathrm{n} > 1,$$

$$L = \frac{\sum_{k=1}^{k=N}\ell_k}{\sqrt{2}},$$

$$A_n = (R-\sum_{k=1}^{k=n}\ell_k)\times\tan\theta,$$

where the N is the maximum intersection before violating the TIR, $\ell_n$ is the travling distance along the propagation direction for the $n_{th}$ intersection, and $A_n$ is the output aperture for the $(n\text{-}1)_{th}$ intersection. The concentration (C) is equal to $(\frac{A_n}{A_1})^2$. A comparison of the length of LC between the calculation and simulation is shown in Figure 62 as $\theta_c = 43.9°, \theta_{in} = 3.9°,\ A = 1.35\,mm$, and θ is from 1.5° to 3°. A smaller θ causes higher concentration, but longer length of the concentrator. Basically, the calculation match with the simulation very well. Althought there exist a slight difference between calculation and simulation, this calculation still can approximate the minimum length of LC by the given parameters. The total concentration in the new design (see Figure 63) is 4781X as $\theta_{in} = 3.9°$ and $\mathrm{L} = 34.25$ mm. Actually, the concentration can go up to even higher, e.g., 20000X, if the L is not limited.

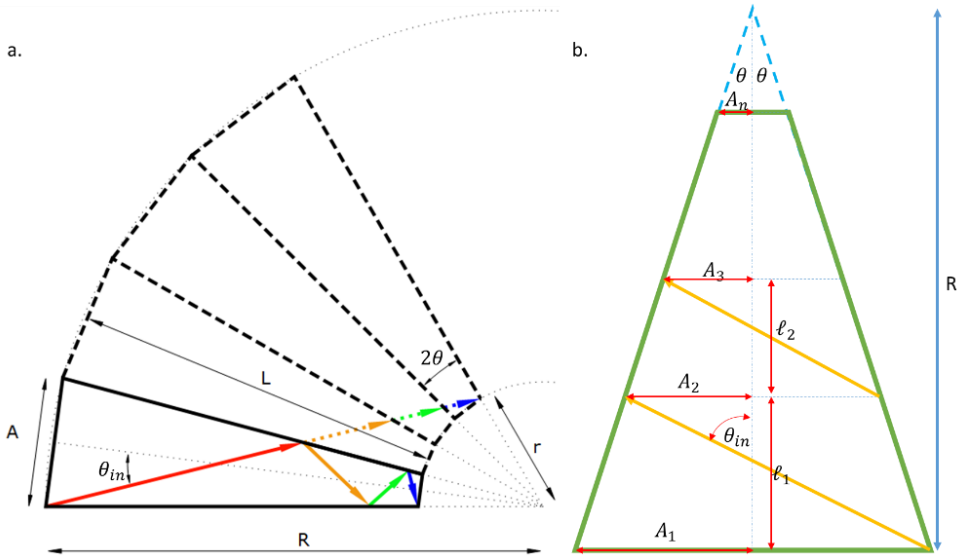


Figure 61. a) The travels inside of the LC can be viewed as the concentrator imaged by its sidewalls. Solid lines are the real propagation path. b) The first intersection inside the LC is not the corner between $\ell_1$ and $A_2$, but rather the corner between $\ell_1$ and $A_1$.

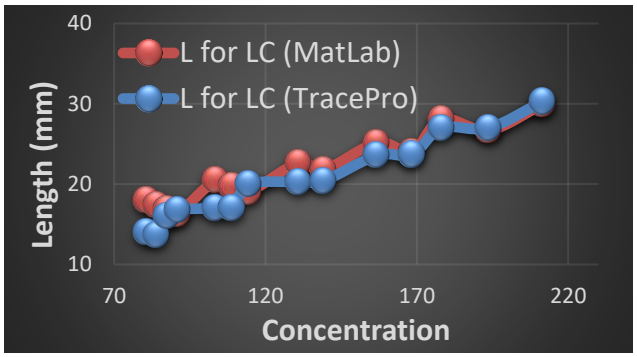


Figure 62. A comparison of the length of LC between the calculation and simulation.

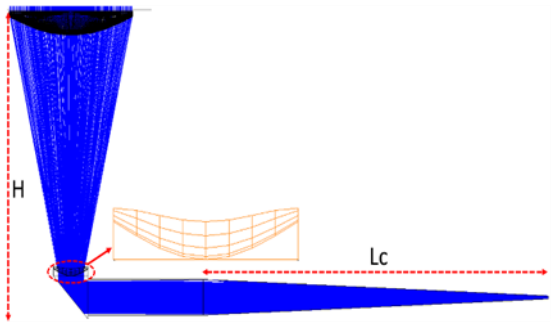


Figure 63. A new CPV design with a linear concentrator and an aspherical concave lens on the 45° prism.

By using these equations of LC, we can calculate the minimum length of LC as C = 1000 for both old and new design (see Figure 64). The area of the first lens is around 100 mm$^2$, so the width of the output aperture is 0.316 mm as C = 1000. The minimum length of LC in the old design is 5.3 mm as $A_1$ = 0.84 mm, $A_n$ = 0.316 mm, and $\theta_{in} = 17°$. For the new design (with a concave

lens), because the distance between two lenses is shorter than the old design the input aperture $A_1$ is increased to 2.7 mm. As C = 1000 and $\theta_{in} = 3.9°$, the minimum length of the LC will be 12.7 mm. Compare to the old design, the minimum length of LC in the new design is 1.96 mm longer than the lens, it means the stretched-out part cannot be totally cover by the next lens, i.e., it will cause a loss. There are two possible method to solve this issue, design a lens has smaller F# or a different type of concentrator. For example, the compound parabolic concentrator.

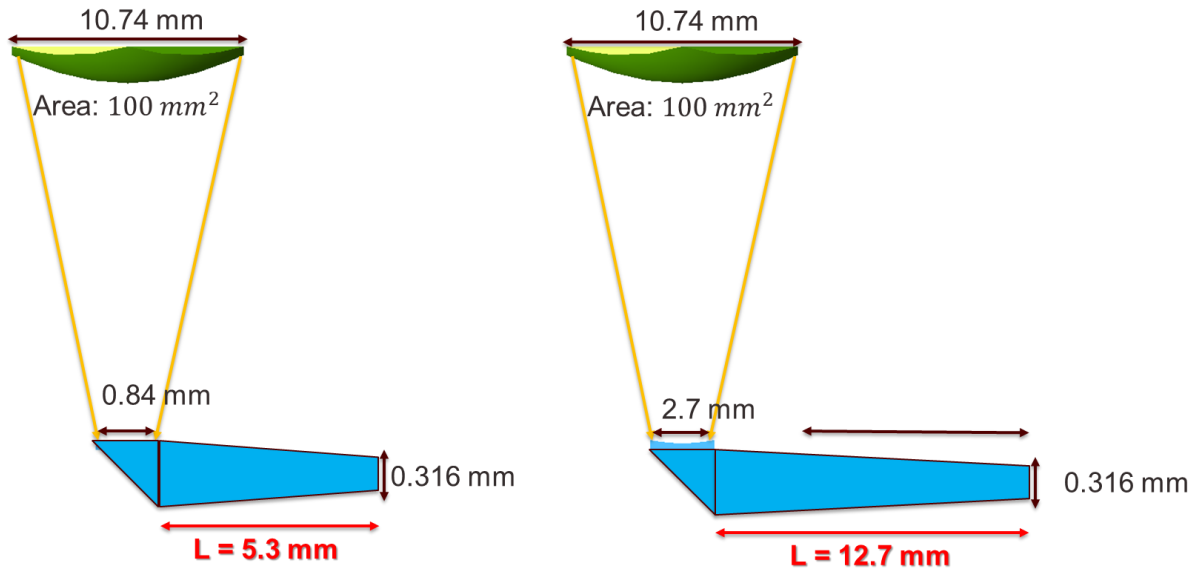


Figure 64. Left side and the right side is the old design and new design, respectively. The structure of the concentrator shown here is different from that shown in the second section.

## 4.3 Compound parabolic concentrator (CPC)

CPC is composed of two parabolic curves that have the same focal length but the different direction of axial symmetry, as the blue and orange curves shown in Figure 65. A unique property of parabolic curve is that if the ray is parallel to the axial symmetry of a parabolic curve, then this ray will hit onto its focal point. The angle, $\theta_{max}$, between the axial symmetry of parabola and CPC

is the maximum acceptance angle for CPC. If the incident angle is smaller than $\theta_{max}$, then it will hit on a point between two focal points. A standard CPC can be designed by

$$f = a(1 + \sin\theta_{max}),$$

$$L = \frac{f \times \cos\theta_{max}}{(\sin\theta_{max})^2} = \frac{A+a}{\tan\theta_{max}},$$

and

$$C = \frac{A^2}{a^2} = \frac{1}{(\sin\theta_{max})^2},$$

where f is the focal length of the parabolic curve, L is the length of CPC, A and a is the input and output aperture, respectively, and C is the concentration.

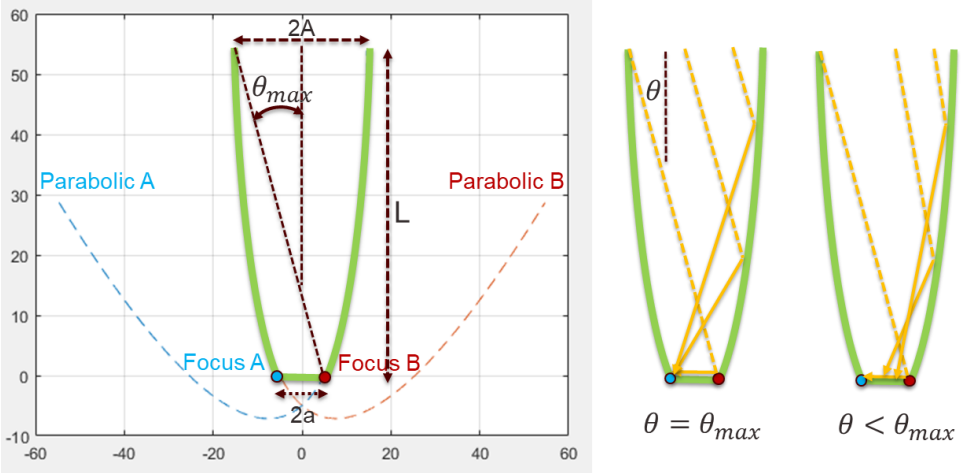


Figure 65. A schematic of CPC. This CPC is designed by $\theta_{max}$ = 10° and a = 1mm. $f = a(1 + \sin\theta_{max}) = 1.1736$ , $L = \frac{f \times \cos\theta_{max}}{(\sin\theta_{max})^2} = \frac{A+a}{\tan\theta_{max}} = 38.33$ and $A = L \times \tan\theta_{max} - a = 5.7588$.

Figure 66 shows a design uses a CPC as the second concentrator. Based on the angular distribution shown in Figure 59, the minimum $\theta_{max}$ for 100% transmission is 3.9°. If A =

1.35 mm, then a = 0.0918 mm, f = 0.098 mm, L = 21.15 mm, and C = 216X (for CPC). The total concentration C = 17 × 216 = 3672X, here 17 is the concentration ratio of the first lens.

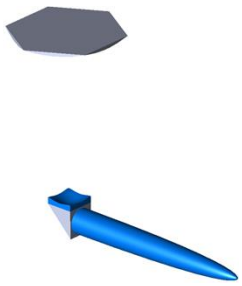

Figure 66. A design with CPC and concave lens.

The design of the aspherical concave lens is a critical process in this section because different parameters will cause different $\theta_{max}$, C and L. Figure 67 shows a trade-off chart for designing the concave lens. In this chart, we can notice that a smaller $\theta_{max}$ has higher concentration but longer length. Although a larger $\theta_{max}$ causes a lower concentration, it has a shorter length and higher tracking tolerance than a small $\theta_{max}$. Figure 68 shows the comparison of tracking tolerance between new and old design.

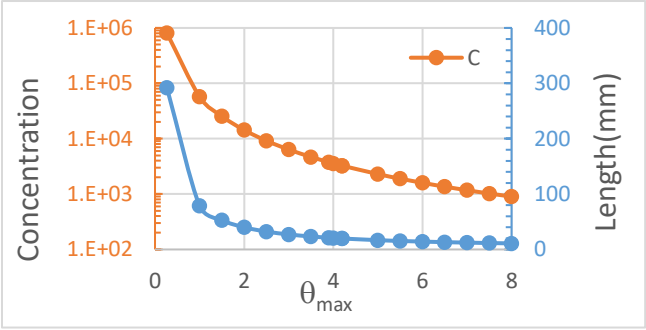


Figure 67. Here, the concentration includes the 1st and 2nd concentrator (CPC).

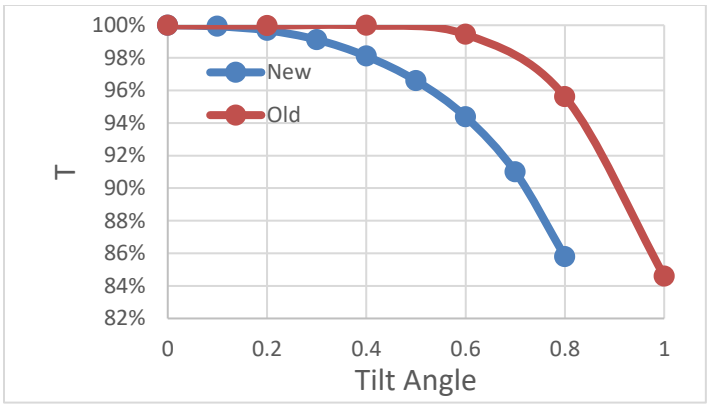


Figure 68. Tracking tolerance between new and old design.

Comparing with a linear concentrator, for achieving the same concentration, the length of CPC is around half of the linear taper as the concentration is higher than 200X (see Figure 69). Another advantage of CPC is that every ray only reflects once inside of CPC no matter what the length is, but the intersections will increase with the length for the linear concentrator. Furthermore, the CPC will only drop around 10% of concentration if we truncate one-thirds its length (see Figure 70).

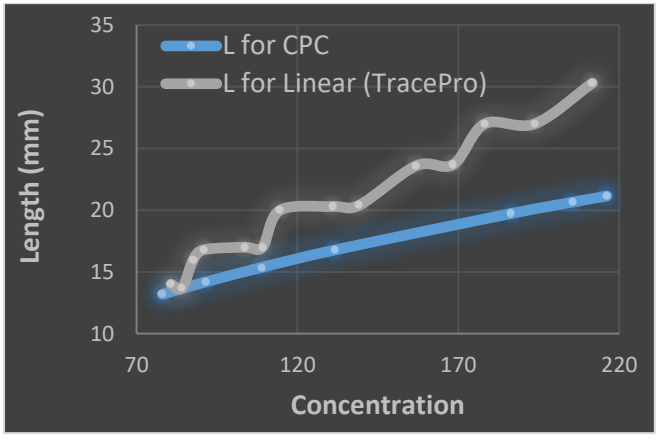


Figure 69. Comparison of the length of concentrator between CPC and LC. Here, the concentration is only for CPC and LC.

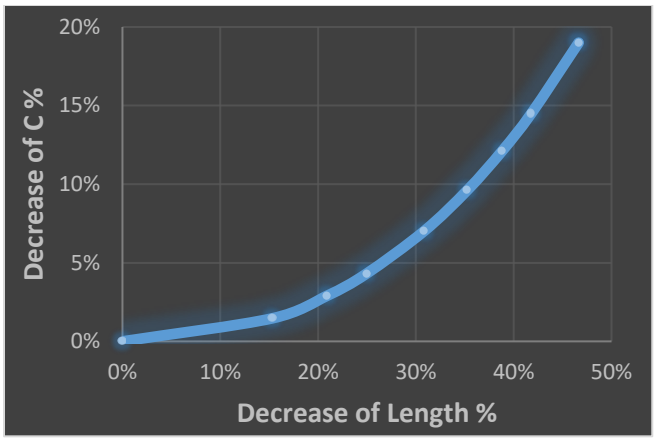


Figure 70. If the length of CPC is decreased by 31%, then the total concentration will be decreased by 7%.

## 4.4 Summary

In this section, we mount an aspherical concave lens on the prism coupler to reduce the loss caused by HR coating and surface roughness. The concave lens decreases the divergence angle from $\pm 17°$ to $\pm 4°$. The loss on the $45°$ surface is less than 1% even if without HR coating. Furthermore, due to the rays are almost parallel with the waveguide, the total intersections inside of waveguide are also dramatically reduced. On the other word, the quality of the surface is not such important to compare with the old design.

The length of LC in this design is longer than the lens so that it will produce a gap between every lens. Therefore, we introduce the CPC to solve this issue. Nevertheless, using CPC will lose a critical advantage of the planar waveguiding CPV base on our design. Because of the curved surface of CPC, the output aperture of every CPC cannot be connected. Actually, the linear concentrator also can achieve the same concentration ratio with CPC, but the length is just longer than CPC.

# 5. CONCLUSION

A manufacturable planar waveguiding solar concentrator is proposed in the first section. This design solves the fabrication issues, e.g., material, technique, and structure, and it achieves the almost all of requirements such as 30% of total harvesting efficiency in low-DNI, 1000X concentration, 90% of optical efficiency, total height < 25mm, and acceptance angle > 0.9°. The only issue we have not overcome yet is the cost. We also discussed the trade-off for different possible designs that can improve partial system performance. For example, an extra concave lens can reduce the loss caused by HR coating and surface roughness, but it also increase the length of the coupler.

For estimating the scattering loss caused by the surface roughness, we investigate the impact from RMS roughness, spatial wavelength, and RMS slope, and we discover the RMS slope is the primary indicator to control the average scattering loss of a light pipe. We compare the simulation result that is based on GO approximation with ABg scattering model and experimental data, and the comparisons show that ABg cannot replace GO approximation. Furthermore, we can match the simulation data with the experimental data by only controlling the RMS slope.

REFERENCES


[1] International Energy Agency (2014). *2014 Key World Energy Statistics*. Available: https://www.webcitation.org/6YIEFsQ6b?url=http://www.iea.org/publications/freepublications/publication/KeyWorld2014.pdf

[2] National Renewable Energy Laboratory. Available: https://www.nrel.gov/pv/assets/images/efficiency-chart.png

[3] G. Sala, "Concentrator Systems," in *Practical Handbook of Photovoltaics (Second Edition)*, ed Boston, MA, USA: Academic Press, 2012, pp. 837-862.

[4] Advanced Research Projects Agency-Energy. (2015). *Micro-scale Optimized Solar-cell Arrays with Integrated Concentration (MOSAIC)*.

[5] K. Shanks, S. Senthilarasu, T. K. Mallick, " Optics For Concentrating Photovoltaics: Trends, Limits And Opportunities For Materials And Design," *Renewable And Sustainable Energy Reviews*, vol. 60, pp. 394-407, 2016.

[6] K.J.Weber, V.Everett, P.N.K.Deenapanray, E.Franklin, A.W.Blakers, "Modeling Of Static Concentrator Modules Incorporating Lambertian Or V-Groove Rear Reflectors," *Solar Energy Materials And Solar Cells*, vol. 90, pp. 1741-1749, 2006.

[7] N. E. Gharbi, H. Derbal, S. Bouaichaoui, N. Said, "A Comparative Study Between Parabolic Trough Collector And Linear Fresnel Reflector Technologies," *Energy Procedia*, vol. 6, pp. 565-572, 2011.

[8] R. Abbas, M. J. Montes, M. Piera, J. M. Martínez-Val, "Solar Radiation Concentration Features In Linear Fresnel Reflector Arrays," *Energy Conversion And Management*, vol. 54, pp. 133-144, 2012.

[9] F. Languy, K. Fleury, C.c Lenaerts, J. Loicq, D. Regaert, "Flat Fresnel Doublets Made Of PMMA And PC: Combining Low Cost Production And Very High Concentration Ratio For CPV," *Optics Express*, vol. 19, issue S3, pp. A280-A294, 2011.

[10] W. G.J.H.M. van Sark, K. W.J. Barnham, L. H. Slooff, A. J. Chatten, A. Büchtemann, "Luminescent Solar Concentrators - A review of recent results," *Optics Express*, vol. 16, issue 26, pp. 21773-21792, 2008.

[11] J. H. Karp, E. J. Tremblay, and J. E. Ford, "Planar Micro-Optic Solar Concentrator," *Optics Express*, vol. 18, pp. 1122-1133, 2010.

[12] Y. Liu, R. Huang, C. K. Madsen, "Design Optimizations For A Lens-To-Channel Waveguide Solar Concentrator," in *2015 IEEE 42nd Photovoltaic Specialist Conference (PVSC)*, New Orleans, LA, USA, 2015.

[13] Y. Liu, R. Huang, C. K. Madsen. "Design Of A Lens-To-Channel Waveguide System As A Solar Concentrator Structure," *Optics Express*, vol. 22, pp. A198, 2014.

[14] C. Hu et al., “High Efficiency Glass Waveguiding Solar Concentrator,” presented at the Photovoltaic Specialists Conference, Washington DC, 26-Jun-2017.

[15] A. Davis, "Fresnel Lens Solar Concentrator Derivations And Simulations," in *Novel Optical Systems Design And Optimization XIV*, San Diego, CA, USA, 2011, pp. 81290J-81290J-15.

[16] Y. Liu, "Designs of a Planar Waveguide Solar Concentrator," Texas A&M University, 2015.

[17] J.-Q. Xi, M. F. Schubert, J. K. Kim, E. F. Schubert, M. Chen, "Optical Thin-film Materials With Low Refractive Index For Broadband Elimination Of Fresnel Reflection," *Nature Photonics*, vol. 1, pp. 176–179, 2007.

[18] Y. Liu, R. Huang, C. K. Madsen, "Two-Axis Tracking Using Translation Stages For A Lens-To-Channel Waveguide Solar Concentrator," *Optics Express*, vol. 22, issue S6, pp. A1567-A1575, 2014.

[19] AZUR SPACE Solar Power GmbH, Cell Type: 3C44 – 3x3mm². Available: http://www.azurspace.com/images/products/0004357-00-01_3C44_AzurDesign_3x3.pdf

[20] SUNPOWER, Cell Type: C60. Available: http://www.sunlife.com.ua/doc/sunpower%20C60.pdf

[21] E.R. Freniere, G.G. Gregory, R.C. Chase, "Interactive Software For Optomechanical Modeling," *SPIE*, vol. 3130, 66. 128, 1997.

[22] F.E. Nicodemus, "Reflectance Nomenclature And Directional Reflectance And Emissivity," *Applied Optics*, vol. 9, issue 6, pp. 1474-1475, 1970.

[23] D. Bergström, J. Powell, A. F. H. Kaplan, "A Ray-Tracing Analysis Of The Absorption Of Light By Smooth And Rough Metal Surfaces," *Journal of Applied Physics*, vol. 101, issue 11, pp. 113504, 2007.

[24] H. Baghsiahi, K. Wang, W. Kandulski, R. C. A. Pitwon, D. R. Selviah, "Optical Waveguide End Facet Roughness and Optical Coupling Loss," *Journal of Lightwave Technology*, vol. 31, no. 16, 2013.

[25] J. T. Remillard, M. P. Everson, W. H. Weber, "Loss Mechanisms in Optical Light Pipes," *Applied Optics*, vol. 31, no. 34, pp. 7232-7241, 1992.

[26] K. Tang, Ralph A.Dimenna, Richard O.Buckius, "The Geometric Optics Approximation For Reflection From Two-Dimensional Random Rough Surfaces," *International Journal of Heat and Mass Transfer*, vol. 41, no. 13, pp. 2037-2047, 1998.

[27] C. Hu, Y. Dogan, and C. K. Madsen, "A Better Predictor for Waveguide Outcoupling by Surface Texturing or Roughness," in Light, Energy and the Environment, OSA Technical Digest (online) (Optical Society of America, 2017), paper RW4A.5.

[28] D. Bergström, J. Powell, A. F.H. Kaplan, "The Absorption Of Light By Rough Metal Surfaces—A Three-Dimensional Ray-Tracing Analysis," *Journal Of Applied Physics*, vol. 103, issue 10, pp. 103515, 2008.

[29] D. Bergström, MySymLab. Available: http://www.mysimlabs.com/about.html

[30] Technical Glass Products, *Fused Quartz/Fused Silica Average Transmittance Curves*. Available: http://www.technicalglass.com/fused_quartz_transmission.html

[31] Spectra-Physics, *Using Femtosecond Laser Irradiation and Chemical Etching (FLICE)* for Waveguide Writing. Available: https://www.azooptics.com/Article.aspx?ArticleID =988

[32] NKT Photonics, *Superk Compact Supercontinuum Lasers (SuperK COMPACT)*. Available: https://www.nktphotonics.com/lasers-fibers/product/superk-compact-supercontinuum-lasers/

[33] R. N. Pfisterer, "Approximated Scatter Models for Stray Light Analysis," *Optics & Photonics News*, pp. 16, 2011.

[34] J. C. Stover, "Optical Scattering: Measurement and Analysis 3rd Edition", SPIE Press, 2012.

[35] J. Irizar, B. Harnisch, " BRDF Prediction Using Surface Micro-Roughness Measurements," *International Conference on Space Optical Systems and Applications*, Ajaccio, Corsica, France, 2012.